



Application of Artificial Intelligence Techniques to Predict Strip Foundation Capacity Near Slope Surfaces

Khalil S. Ismael¹ · Rafi' M. Sulaiman Al-Ne'aimi¹

Received: 19 August 2023 / Accepted: 9 October 2023 / Published online: 12 November 2023
© The Author(s), under exclusive licence to Indian Geotechnical Society 2023

Abstract In some situations, a foundation is built on or near the crest of a slope. As a result, the soil's overall stability and bearing capacity dramatically reduced, depending on many geometrical and geotechnical factors. This study consists of two main parts: numerical analysis and artificial intelligence prediction. In the numerical section, simple two-dimensional numerical models have been employed using Plaxis 2D software to examine the bearing capacity and slope stability of a continuous foundation placed near a slope. It specifies foundation width and depth, soil cohesion, frictional and slope angles, and slope crest distances. A comprehensive database of simulated results was used to develop and validate ANN and EPR prediction expressions as well as the relevance of the input parameters. The results show that there is a positive relationship between all studied variables and $(q_u/\gamma H)$ except the slope angle β . The FOS increases as the footing distance away from the slope edge increases up to a critical b/B ratio; LE methods, however, yield a higher FOS value than FEM as a result of their differing approaches. It was determined that the essential distance between the slope crest and the continuous foundation edge is $6B$ after which the slope's impact diminishes. Based on the input variables sensitivity analysis, B , ϕ , and c were identified as the most effective input parameters. Finally, as a result of the case study analysis, the authors concluded that both ANN and EPR models are highly accurate with

differences within 6%. The ANN model is superior to EPR but lacks a straightforward mathematical solution.

Keywords ANN · Bearing capacity · EPR · Finite element · Slope surface · Strip footing

List of Symbols

a_j	Constant
b_o, b_{hN}	The output and Nth hidden layer bias Biases
$ES_{k \times m}$	Matrix of exponents
f_{sig}	Tan-sigmoid transfer function
h	Hidden layer neurons
Hidden _{XN}	Absolute connection weight values for input to output nodes
Hidden _{ZN}	Absolute product connection weight values for the input-hidden and hidden-output nodes
m	Power for a stress-level dependency on stiffness
m	Input variables number
m	Number of terms of the target expression
N_1, \dots, N_5	Hidden layer nodes
P_i^a, P_i^n	The ith. input or target vector components before and after normalization
P_i^{\max}, P_i^{\min}	Max. and Min. values before normalization of all input or target vector components
$q_u/\gamma H$ or $(q_u/\gamma H)_{\text{norm}}$	Normalized bearing capacity
$(q_u/\gamma H)_{\text{denorm}}$	De-normalized bearing capacity
R	Correlation coefficient
X_1, \dots, X_6	Input variables
Y	Target or output

✉ Khalil S. Ismael
khalil.sadiq@uod.ac

Rafi' M. Sulaiman Al-Ne'aimi
rafi.mahmoud@uod.ac

¹ Civil Engineering Department, University of Duhok, 1006 Duhok, Iraq

$Y_{N \times 1}(\theta, Z)$	The least squares vector of the N target values
$\theta_{1 \times d}$	Vector of $d = m + 1$ parameters a_j and a_0
θ^T	Transpose vector of parameters set
Ψ	Dilatancy angle
ω_{iN}	Related weight between the i th input layer and Nth hidden layer nodes
ω_N	Related weight between Nth hidden layer node and output node
$Z_{N \times d}$	A matrix formed by I (unitary vector) for bias a_0 , and m vectors of variables Z^j
Z^j	Jth column vector whose elements are products of the candidate independent inputs, $X = \langle X_1, X_2, \dots, X_k \rangle$

Abbreviations

AI	Artificial Intelligence
ANN	Artificial Neural Network
COD	Coefficient of Determination
EPR	Evolutionary Polynomial Regression
EX	User-defined vector
FEM	Finite Element Method
FFBP	Feed-Forward–Backward Propagation
FOS	Factor of safety
GP	Genetic Programming
HS	Hardening soil model
HS _{small}	Hardening soil model with small-strain stiffness
LEM	Limit Equilibrium Method
LE	Linear elastic model
LS	The linear least squares method
MAE	Mean Absolute Error
MC	Mohr-Coulomb model
MSE	Mean Squared Error
NAES	Non-dimensional Average Element Size
RMSE	Root Mean Square Error
SSE	The sum of squared errors
TRIANLM	Levenberg–Marquardt training function

Introduction

Bearing capacity (BC) and settlement estimation are key factors for geotechnical engineers to consider when designing a foundation. These design requirements are affected by the

geotechnical properties of the soil, the geometric characteristics of the footing, and the loading circumstances. However, due to the variability and anisotropy of soil formation, numerous methodologies have been developed to assess the BC of foundations on level ground under different circumstances [1, 2]. The foundation should be designed with an appropriate safety factor against shear collapse and permissible foundation settling. In hilly areas, the construction of the foundation on the slope is unavoidable. However, due to fast urbanization and population increase, many commercial or residential structures, such as bridge abutments, electric and mobile transmission towers, buildings, and elevated water tanks, will be located on or near the crest of earthen slopes. As a result, the behavior of the foundation on the slope crest/face will alter in terms of BC and overall structural stability. The established passive resistance zone towards the slope's face will reduce depending on the footing location from the slope edge and thereby the carrying capacity of earth slope footings will be less than that of level ground footings.

Several studies have published several methodologies and approaches for estimating the bearing resistance of foundations situated on earthen slopes. These strategies include experimental model testing [3, 4]; theoretical and analytical research [5–8]; and numerical methods [9–11]. Artificial intelligence (AI) methods, particularly Artificial Neural Networks (ANNs) and Evolutionary Polynomial Regression (EPR), are now widely used in geotechnical engineering for their superior prediction abilities in simulating complex material behavior. Researchers in geotechnical engineering have utilized ANN and EPR techniques since the 1990s in foundation engineering, specifically to assess settlement [12, 13] and estimate BC of individual shallow foundations resting on level ground [14–16].

Further, a broad variety of parameters have been studied using various hybrid learning models; such as the GWO-RF model to predict the splitting tensile strength of recycled aggregate concrete with glass fiber and silica fume [17]; PSO and BWOA techniques for predicting pavement material resilient modulus (MR) under wet-dry cycles [18]; PSO-RF and HHO-RF models to forecast pile set-up parameter 'A' from CPT. However, HHO-RF is more efficient than PSO-RF, with R^2 and RMSE both equal to 0.9328 and 0.0292 for training and 0.9729 and 0.024 for test data, respectively [19]. All these prediction models aligned with experimental results using various assessment criteria and techniques, such as error criteria, Taylor diagrams, uncertainty analysis, scatter index analysis, and error distribution.

Some researchers used the ANN and EPR to estimate the bearing capacity (BC) on the sloped ground [10, 20–22], while others have applied EPR to evaluate various geotechnical engineering applications [23–25]. Nevertheless, in 2021, only Ebid et al. [22] used EPR to estimate BC factors for a strip foundation near an earthen

slope crest using Meyerhof's approach. EPR models are offered in mathematical expression forms, making them simply accessible to the modeler. As a novel aspect of this study, two models have been constructed, utilizing ANN and EPR, to estimate BC on sloped grounds, which was not attempted in previous studies by Acharyya and Dey [21] and Acharyya et al. [10]. The current work seeks to examine the BC of individual continuous foundations set on an earthen-sloping crest through a comprehensive numerical analysis utilizing the PLAXIS 2D v20 finite element software. Many geometrical and geotechnical variables were investigated to achieve the study's objectives, including footing width (B), soil cohesion (c), soil friction angle (ϕ), footing embedment (D_f/B), slope angle (β) and setback distance (b/B). Based on the parametric analysis results, two models were developed using ANN and EPR techniques to construct a mathematical expression for estimating the BC of individual continuous foundations placed on an earthen slope. Further, to determine the relative relevance of the input parameters, a sensitivity analysis was performed on each model. These approaches greatly assist design and consulting engineers in estimating BC quickly and easily.

Method of Analysis

Model Geometry, Boundaries, and Meshing

As illustrated in Fig. 1, the slope model geometry was chosen so that isobar stresses would not reach the model's borders. The model boundaries are selected with the bottom boundary fully rigid and restricted in both vertical and horizontal directions. The vertical boundaries are fixed horizontally, but vertical deformation is allowed, while the slope face is kept free from movement.

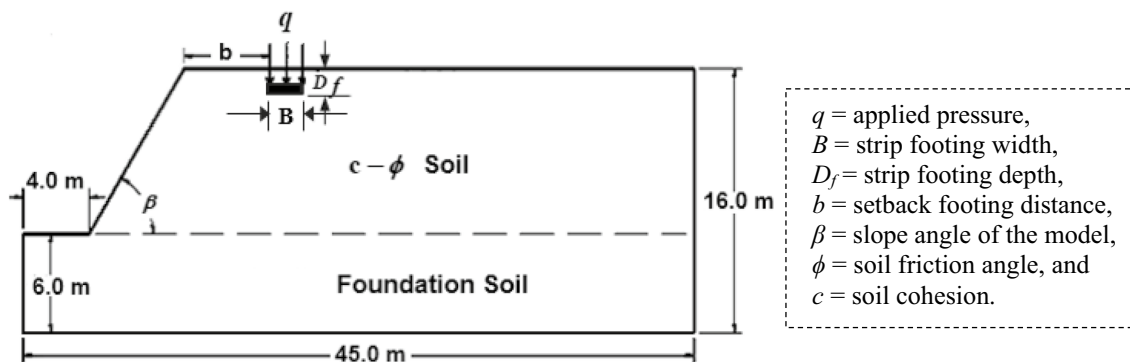


Fig. 1 Model geometry

Sensitive Analysis

The model is divided into finite elements for numerical analysis. The mesh must be fine for reliable results. A coarse mesh hinders capturing soil and foundation characteristics. A fine mesh creates more elements and requires longer processing time. Hence, a sensitivity analysis was done to determine the ideal mesh size for the FE model, considering PLAXIS meshing options. These meshes are categorized as very coarse, coarse, medium, fine, and very fine. To reduce reliance on the numerical model, the optimal mesh element size is determined using non-dimensional average element size (NAES). Figure 2 shows how the elements' size affects the bearing pressure of the strip foundation on the earth's slope. A fine meshing approach with NAES of 0.04 yielded favorable results and was used in the current numerical model study. After properly defining soil, foundation, loads, and slope boundaries, automatic mesh generation is done. Figure 3 shows the geometry and meshing of the Plaxis 2D FE model.

Constitutive Modeling

The hardening soil model with small-strain stiffness (HSsmall) is used to simulate backfill and foundation soils. It is an expansion of the hardening soil (HS) model, considering increasing soil stiffness at low strains. Most soils have more stiffness at small strain levels than at engineering strain levels, and this stiffness changes non-linearly with strain. This behavior is given in the HSsmall model by two extra material parameters, G_0^{ref} , and $\gamma_{0.7}$ where G_0^{ref} is the small-strain shear modulus and $\gamma_{0.7}$ is the strain level at which the shear modulus has decreased to approximately 70% of the small-strain shear modulus. This model has a cap yield surface (see Fig. 4) and accurately reproduces soil deformations better than other models because of its non-linear stress–strain relationship and calculated soil stiffness using various loading and

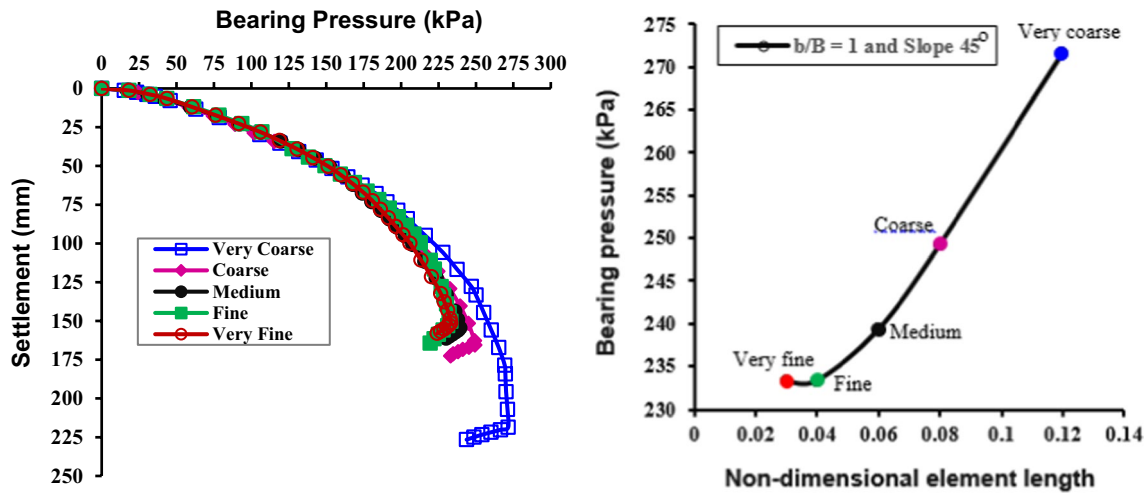


Fig. 2 Mesh sensitivity

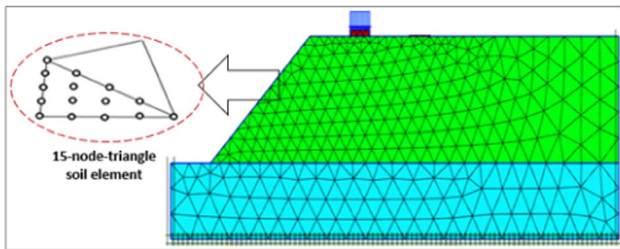


Fig. 3 Mesh generation and boundary fixation

unloading techniques [26, 27]. This study uses 15-node triangular elements with 2 degrees of freedom per node for modeling soil elements. These elements have 12 stress points, providing quicker convergence and more accurate results compared to 6-noded elements. The linear elastic (LE) model has been used for modeling the concrete foundation. Tables 1 and 2 display the soil and concrete foundation parameters employed in this study.

Finite Element Software and its Validation

In this work, PLAXIS 2D v20 software is used for numerical modeling and analysis. The software is a professional finite element package for the deformation and stability analysis issues in geotechnical engineering concerns such as tunnels, earth structures, deep excavations, etc. Many researchers have successfully utilized this program to explore the foundation behavior on earth slopes, bearing capacity, and slope stability evaluation [28–30].

To ensure PLAXIS accuracy in analysis, the findings of Abed and Hameed’s [31] numerical analysis using PLAXIS 3D and the experimental work described by Lee and Manjunath [32] for a strip foundation set on an earth slope were used to verify the FE model. The comparison of analytical results in terms of load-deformation curves, as illustrated in Fig. 5a, revealed a close agreement in terms of both magnitude and trend. Furthermore, the assessment of the slope stability of the present numerical analysis is verified with the

Fig. 4 a Different moduli of typical stress–strain HS small soil model, b The cap yield surface in principle stress space

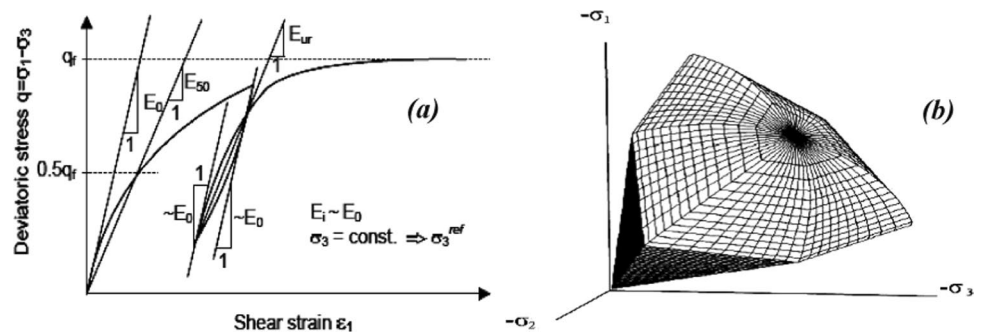


Table 1 Soil properties

Parameters	Name	Backfill material	Foundation material	Unit
Material model	–	HS _{small}	HS _{small}	–
Material behavior type	–	Drained	Drained	–
Unsaturated soil unit weight	γ_{unsat}	16	20	kN/m ³
Saturated soil unit weight	γ_{sat}	18	20	kN/m ³
Secant stiffness in standard drained triaxial test	E_{50}^{ref}	3.0×10^4	3.0×10^4	kN/m ²
Tangent stiffness for primary oedometer loading	E_{oed}^{ref}	3.601×10^4	3.0×10^4	kN/m ²
Unloading/reloading stiffness	E_{ur}^{ref}	1.108×10^5	1.2×10^5	kN/m ²
Power for a stress-level dependency on stiffness	m	0.5	1	–
Cohesion	c_{ref}	variable	40	kN/m ²
Friction angle	ϕ	variable	24	°
Dilatancy angle	ψ	$\phi - 30$	0	°
Shear strain at which $G_s = 0.722 G_0$	$\gamma_{0.7}$	1.5×10^{-4}	1.0×10^{-3}	–
Shear modulus at very small strains	G_0^{ref}	1.0×10^5	1.0×10^5	kN/m ²
Poisson’s ratio	ν'_{ur}	0.2	0.2	–

Table 2 Foundation properties

Parameters	Concrete foundation	Unit
Material model	Linear elastic	–
Material behavior type	Non-porous	–
Concrete unit weight, $\gamma_{conc.}$	24	kN/m ³
Young’s modulus, E'	25×10^6	kN/m ²
Poisson’s ratio, ν	0.15	–

Limit Equilibrium Method (LEM) results conducted by [33]. The verification results exhibit good indication as illustrated in Fig. 5b. Thus, the verified model can be utilized for conducting a parametric study to explore the numerous design parameters’ impact on the bearing pressure of a single strip foundation situated on a sloped soil surface.

Artificial Intelligence (AI) Techniques

Artificial Neural Networks (ANNs) Approach

ANNs are mathematical tools and data processing systems used to express complex, nonlinear processes by connecting inputs and outputs. They consist of interconnected neurons that are arranged in layers and are connected within each layer by weights. ANNs are suitable for modeling the complex behavior of most geotechnical engineering materials with high variability, as they do not require making hypotheses about fundamental laws and have an advantage over traditional modeling methods.

The dataset is divided into three divisions: training, validation, and testing, each taking a percentage of the total input data. Weights are adjusted at the training stage until desired outputs are achieved. After the training phase is complete, validation data are used to assess the model’s

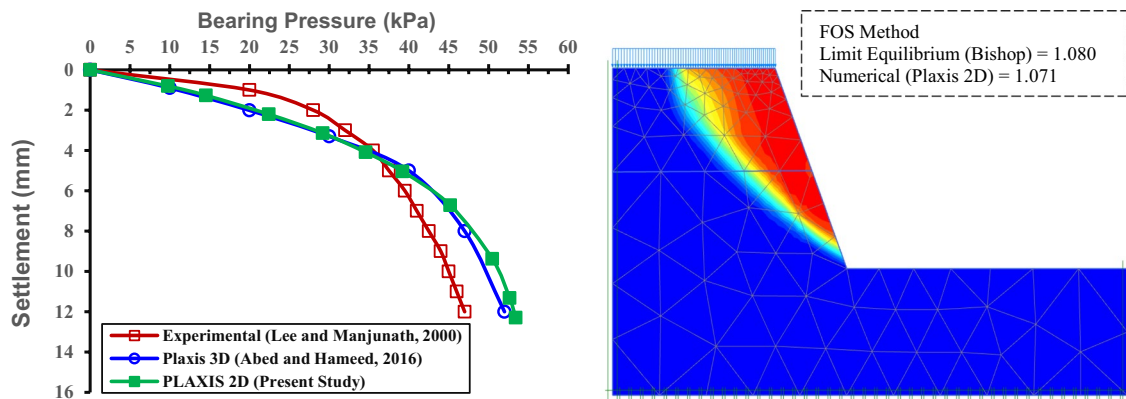


Fig. 5 Verification of the numerical model

performance, and the testing dataset is used to find the ideal hidden layer node numbers.

There are several types of ANNs. The multilayer perceptron network model is one of the most frequent and frequently used network models, with three layer types: input, hidden, and output layers. The proposed network's input layer receives data, which is processed in the hidden layer(s), and the result is transferred to the output layer. The feed-forward-backward propagation (FFBP) algorithm is one of the most essential types of algorithms utilized in the ANN process [34, 35]. In this technique, the ANN must be fed input and output samples. The error-prone FFBP algorithm predicts data output and compares it to the actual output. When there is a mistake, the weights and biases of the various levels are reversed from the output layer to the input layer. This technique is repeated until the ANN error is as close to zero as possible. The network with the highest (R) value and the lowest error value gives the best ANN model, as judged by several metrics such as the correlation coefficient (R), Mean Squared Error (MSE), Root Mean Square Error (RMSE), Mean Absolute Error (MAE), and so on. The number of nodes in the hidden layer(s) is sensitive to the ANNs. Therefore, it should be optimal to maximize the performance of the network; very few nodes may cause underfitting, meanwhile, many nodes may cause overfitting, i.e., the training data will be modeled well, and the sum of the squared errors will be low, but the ANN will be modeling the noise in the data. As a result, the ANN's testing data will be poorly generalized [36]. The general stepwise of the ANN model used in this investigation is shown in Fig. 6.

Evolutionary Polynomial Regression (EPR) Technique

EPR is an AI approach based on evolutionary computing, combining the least squares method and Giustolisi and Savic's Genetic Algorithm (GA) to find optimal and simple scheme descriptions [37]. Unlike ANNs, EPR generates symbolic and straightforward mathematical models [38]. The EPR approach's fundamental features can be expressed in two steps. First, the optimum model architecture in polynomial expression form is chosen using an evolutionary seeking technique via genetic algorithms [39]. Second, numerical regression is performed using the least-squares technique.

Before beginning the EPR operation, some variables need to be modified to regulate the modeling architecture development process. These variables can be utilized to influence the optimization approach employed, such as the exponent ranges, the desired terms number in the mathematical model(s), mathematical structures, and the function types to generate the models. Applying the optimization process, EPR finds the most accurate symbolic model(s) of

the studied system using the stated parameters and the optimization procedure.

Following calibration of the EPR model(s), the best (optimal) model(s) from the chain of returning models can be chosen. The proposed EPR model(s) performance during the testing, validation, and training phases can be evaluated using analytical standard criteria (statistical measures) such as the correlation coefficient R, Coefficient of Determination ($COD = R^2$), Mean Squared Error, MSE, and Root Mean Squared Error, RMSE [37]. The steps of the EPR method and the way it was applied in the study are illustrated in more detail by the flow chart shown in Fig. 7.

Results and Discussion

Numerical Results

Table 3 highlights the diverse geometrical and geotechnical soil variables utilized in the present research for the single-strip foundation model presented in Fig. 3 to calculate the normalized bearing capacity $q_u/\gamma H$ of a continuous foundation positioned on an earthen slope crest corresponding to a settlement of 5%B. The stated statistical information for all used data is presented in Table 4. The histograms combined with the normal distribution curve for inputs and output parameters are shown in Fig. 8.

Effect of Slope Angle and Foundation Setback

The effect of the foundation position b/B from the slope edge and the slope angle β on the $q_u/\gamma H$ of a continuous foundation built on an earthen slope crest is depicted in Fig. 9. This graph illustrates that as the inclination of the slope increases, the $q_u/\gamma H$ value decreases. This is due to the free flow of dirt on the slope surface outward and a reduction in soil confinement or passive resistance from the side slope, which results in a decrease in footing bearing pressure. The outcomes show that the $q_u/\gamma H$ value is strongly related to the b/B ratio up to a critical ratio. Hence, at a small setback distance ratio, slope instability increases, soil confinement, and passive resistance decrease, and the footing-soil system stiffness is adversely affected, resulting in a drop in bearing pressure. The slope angle impact fades away at around $b/B = 6$, and the $q_u/\gamma H$ does not vary significantly for the further b/B ratio. This conclusion supports the findings arrived by [20, 21]. Furthermore, the $q_u/\gamma H$ improvement rate is greater on steep gradient slopes than on low (gentle) gradient slopes.

Effect of Soil Cohesion

Figure 10 highlights the combined impact of the soil cohesion c variation and the b/B ratio on the $q_u/\gamma H$; it shows

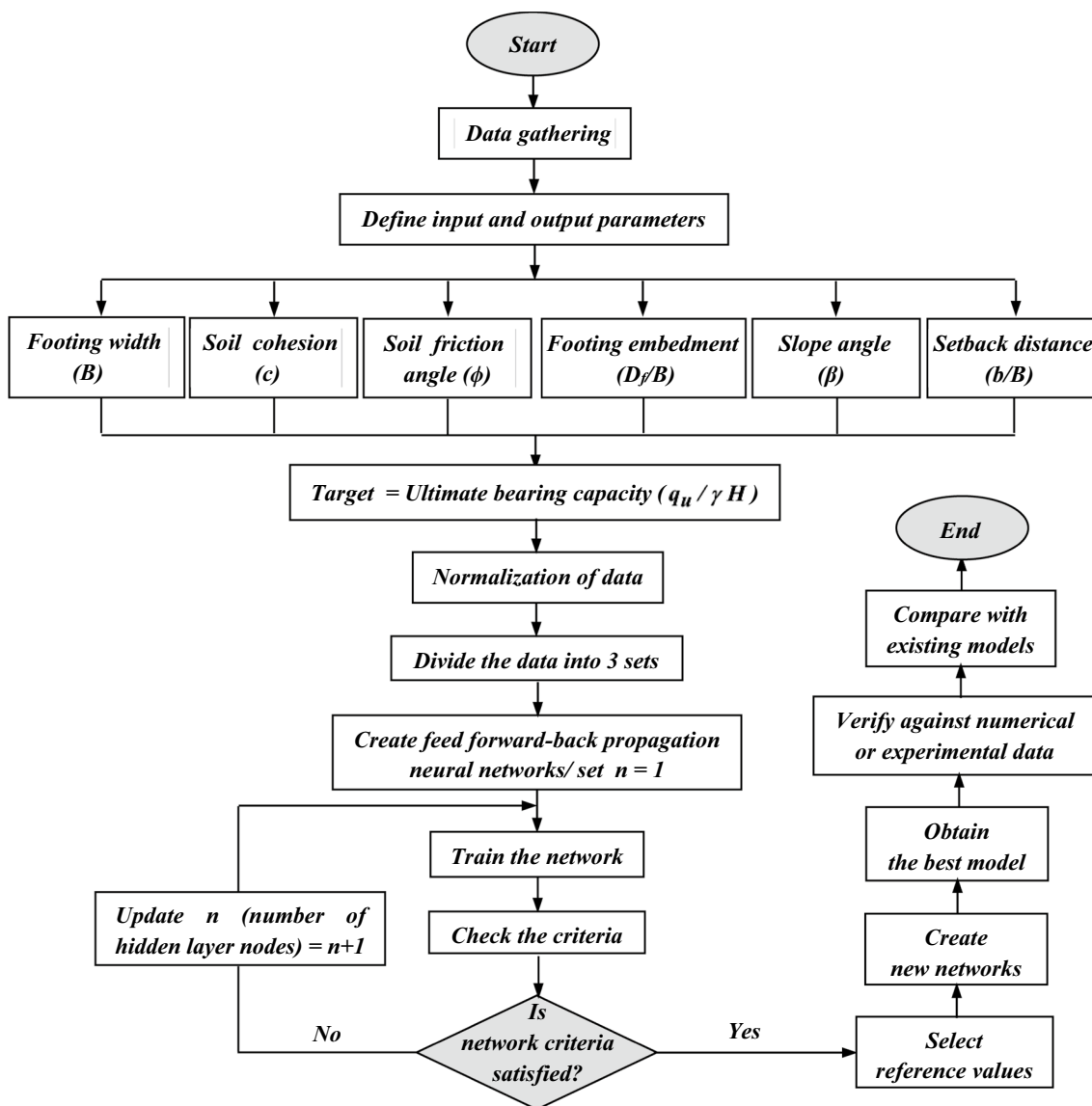


Fig. 6 Flow chart of the utilized ANN model for predicting the ultimate bearing capacity of strip footings

that both have considerable influence on the $q_u/\gamma H$ value. It depicts that the c and b/B ratio positively correlates with the $q_u/\gamma H$ magnitude, the enhancement in the $q_u/\gamma H$ becoming insignificant after $b/B=6$, and the impact being more tangible at larger c values. Improvement of $q_u/\gamma H$ satisfies the reality that increases in soil cohesion include improvements in the shear resistance of the foundation soil.

Friction Angle Impact

Figure 11 depicts the combined effect of the friction angle ϕ and b/B ratio on $q_u/\gamma H$ value; both significantly impact the $q_u/\gamma H$. It is claimed that the ϕ and b/B ratio have a proportionate relationship with the $q_u/\gamma H$ value, the increase in the $q_u/\gamma H$ being inefficient after $b/B=6$, and the impact

became more pronounced at higher ϕ values. The increase in $q_u/\gamma H$ confirms that the changes in soil friction angle increase foundation soil shear resistance.

Embedment Depth Impact

Figure 12 depicts the combined influence of the footing embedment depth D_f/B and the b/B ratios, both of which have a significant effect on the $q_u/\gamma H$ value. It is revealed that increasing of D_f/B and b/B ratios increases the $q_u/\gamma H$ value. This is due to rising soil confinement, which raises the passive resistance zone. Furthermore, increasing $q_u/\gamma H$ value becomes invaluable after $b/B=6$ and has a greater influence at a higher D_f/B ratio.

Fig. 7 EPR-MOGA analysis flow chart [40]

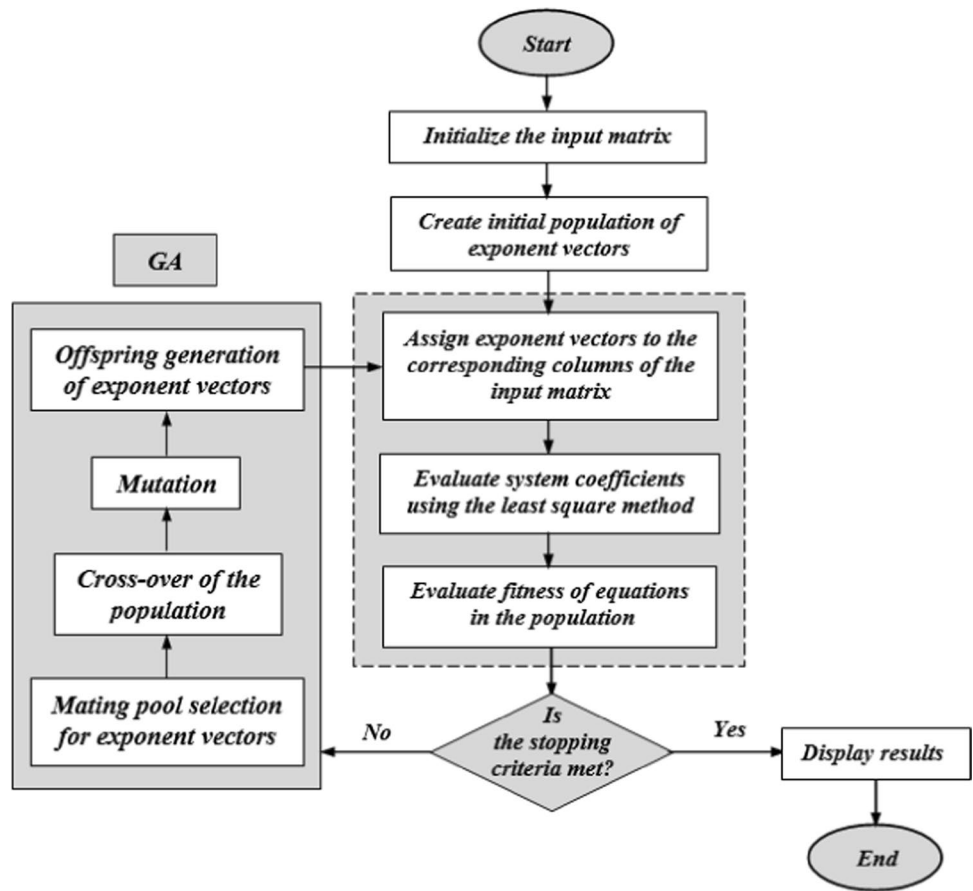


Table 3 Used variables in the numerical analysis

$q_u / \gamma H$								
B (m)	c (kPa)	ϕ°	D_f/B	β°	b/B	No.		
1 2	0	32	0.0 0.5 1.0	35	0 1 2 3 4 5 6 7	48		
		36		35,40		96		
		40		35,40,45		144		
	8	32		35,40,45,50		192		
		36,40		35,40,45,50,60		480		
		15		32,36,40		35,40,45,50,60	720	
	20	32,36,40		35,40,45,50,60		720		
	30	12		35, 40,45		144		
	30	18,25,32		35,40,45,50,60		720		
	40	12		35,40,45,50		192		
		18,25		35,40,45,50,60		480		
		Total dataset					3936	

Effect of Foundation Width

Figure 13 shows the combined impact of the foundation width B and b/B ratio on the $q_u/\gamma H$ value; it reveals that both have a significant effect on the $q_u/\gamma H$ value. The results

observed that when the B and b/B ratio increased, so did the $q_u/\gamma H$ value, since a higher soil depth beneath the foundation contributed to its ability to sustain the applied load. Because soil collapse at a small b/B ratio is caused by a combination of bearing capacity and slope instability failure, the

Table 4 Statistical information of input and target data used in ANN and EPR models

	Input parameters						Target
	B (m)	c (kPa)	ϕ°	D/B	β°	b/B	$q_u/\gamma H$
Minimum	1	0	12	0	35	0	0.104
Maximum	2	40	40	1	60	7	5.548
Mean	1.5	21.183	30.317	0.5	44.883	3.5	2.352
Median	1.5	20	32	0.5	45	3.5	2.245
Standard deviation	0.5	12.137	8.864	0.408	8.307	2.292	1.013
Skewness	0	0.088	-0.765	0	0.567	0	0.502

influence is more noticeable for larger b/B ratio; however, this increases in the $q_u/\gamma H$ value diminished after $b/B=6$.

Effect of Type of Soil

Figure 14 depicts the combined effect of soil shear strength parameters, c , ϕ , and b/B ratio on the $q_u/\gamma H$ value. In general, for any soil type as the b/B ratio increases away from the slope crest the $q_u/\gamma H$ increases up to $b/B=6$. In contrast, for constant b/B , soil B ($c=30$ kPa, and $\phi=32^\circ$) shows the highest $q_u/\gamma H$ value in comparison to soil A which has the lowest cohesion ($c=8$ kPa) although ($\phi=40^\circ$). This demonstrates that the internal friction angle has more effect than soil cohesion. In other words, soil C shows the lowest $q_u/\gamma H$ value resulting from (a decreased internal friction angle of 12° although the cohesion is increased to 40 kPa).

Slope Stability

Figure 15 depicts the safety factor with the b/B ratios. It clearly showed that the FS increases as the b/B ratio increases up to $b/B=3$ and 6 for a 100 kPa loading and a pressure corresponding to 5% B settlement, respectively. After that, the slope effect disappears and the FS and the critical footing setback greatly depend on the applied load. This is due to the rise in the passive confining zone as the foundation moved away further from the slope edge, as previously indicated.

Failure Mechanism

In the current research, the soil failure pattern generated beneath a continuous foundation placed on the slope crest has been analyzed for various β and b/B ratios to determine the key b/B ratio; then, the impact of the β fades away. Figure 16 displays how the slope affects the passive zone formed under the foundation and that the failure pattern is one-sided only and toward the slope direction up to $b/B=6$, affecting the soil bearing pressure and overall slope stability. The failure mechanism established at $b/B \geq 6$ is analogous to the failure mechanism developed on level ground or flat topography.

ANN Model Results

In the current research, the varied parameters listed in Table 3 are used as input data to predict the $q_u/\gamma H$ output of a continuous foundation situated on the slope crest by applying the ANN tool available in MATLAB software, which provides many training functions and algorithms. The FFBP algorithm with Levenberg–Marquardt (TRIANLM) training function has been found efficient in the training process [35], and therefore, it is used to build the ANN model. Table 5 shows how the samples for training, testing, and validation are distributed using random division by the ANN “dividerand” function.

To assess the ANN performance, its predicted results, and the optimal hidden layer nodes (neurons), the R^2 and MSE criteria are considered based on trial and error. According to this analysis, the ANN structure that best fits predicted, and numerical results comprises a 6–5–1 architecture (see Table 6 and Fig. 17).

ANN structure performance

Figure 18 depicts the outcome of the $q_u/\gamma H$ training, validation, and testing processes in agreement with their magnitudes obtained from the FE simulation and those predicted by the ANN model, with R^2 values of 0.996, 0.995, and 0.996, respectively. Thus, Tables 7 and 8 listed the optimal connection weights and biases among ANN layers acquired due to the training process and then employed in both the testing and validation stages.

First, the trained ANN model was coupled with the validation group data, which had been unused during both the training and testing processes, to create the ANN model. The validation phase process is useful in determining whether the ANN model can generalize the physical problem outcome. Figure 18b shows a superior match between those simulated by FE and the estimated $q_u/\gamma H$ magnitudes, emphasizing the best generalization capacity and performance of the 6–5–1 ANN model architecture (see Fig. 19). Second, the trained ANN model and its optimum related weights and biases are considered for the testing phase to check the prediction capacity of the network. Figure 18c indicates a good match

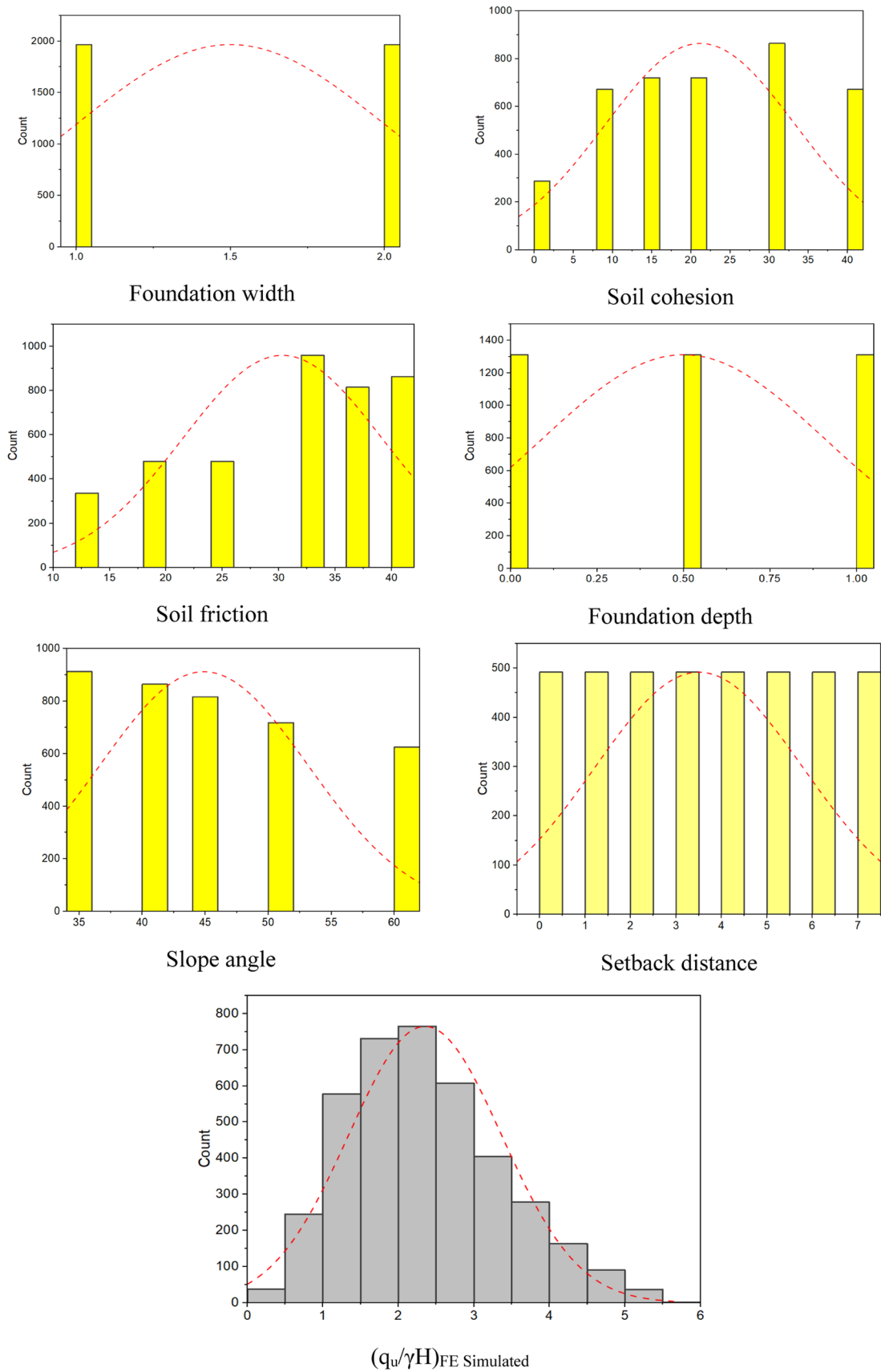


Fig. 8 Histograms and normal distribution curves for input/output parameters

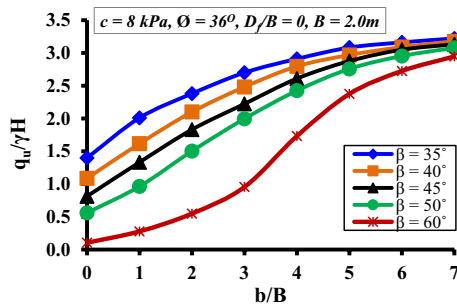


Fig. 9 Combined influence of β and b/B ratio on $q_u/\gamma H$

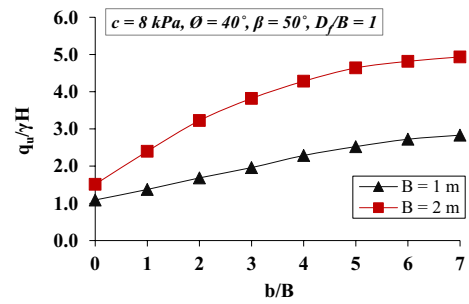


Fig. 13 Effect of B and b/B ratio on $q_u/\gamma H$

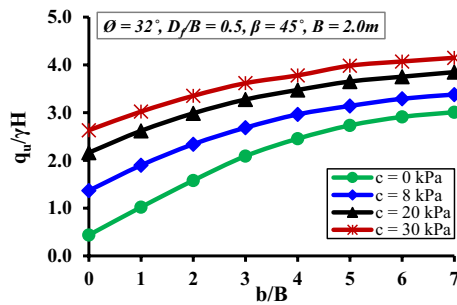


Fig. 10 Impact of c and b/B ratio on $q_u/\gamma H$

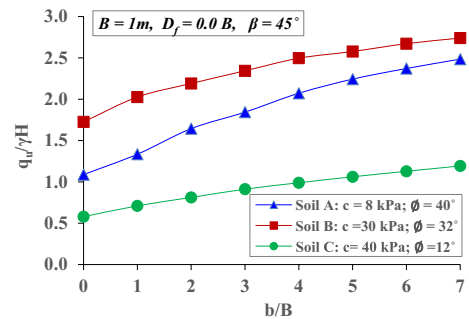


Fig. 14 Combined influence of c , ϕ , and b/B on $q_u/\gamma H$

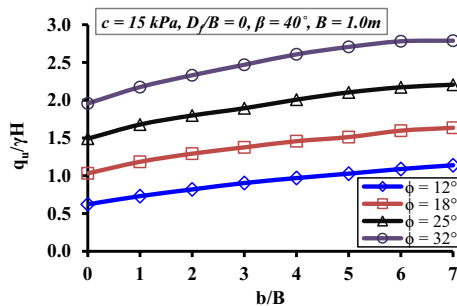


Fig. 11 Effect of ϕ and b/B ratio on $q_u/\gamma H$

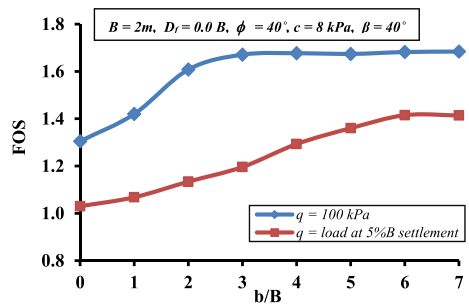


Fig. 15 FOS with b/B ratio

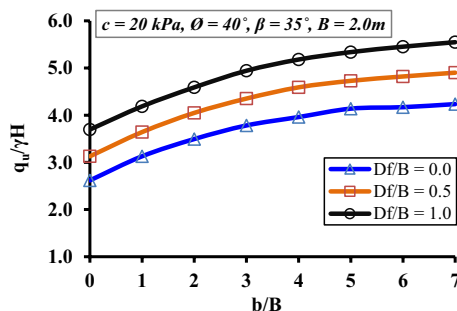


Fig. 12 Effect of D/B and b/B ratios on $q_u/\gamma H$

between the FE simulation outcomes and those predicted by the ANN model. The high R^2 value in the testing phase demonstrates a certainty that the trained ANN has excellent prediction ability.

Input Parameter's Importance

The research required to sort the input factors, highlighting their prioritized impact on the specific physical problem outcome, is known as "sensitivity searching." Such research helps in the "design of experiments" when a large number of physical or numerical simulations are needed, but only a few of them are chosen for real modeling due to the sensitive effect of

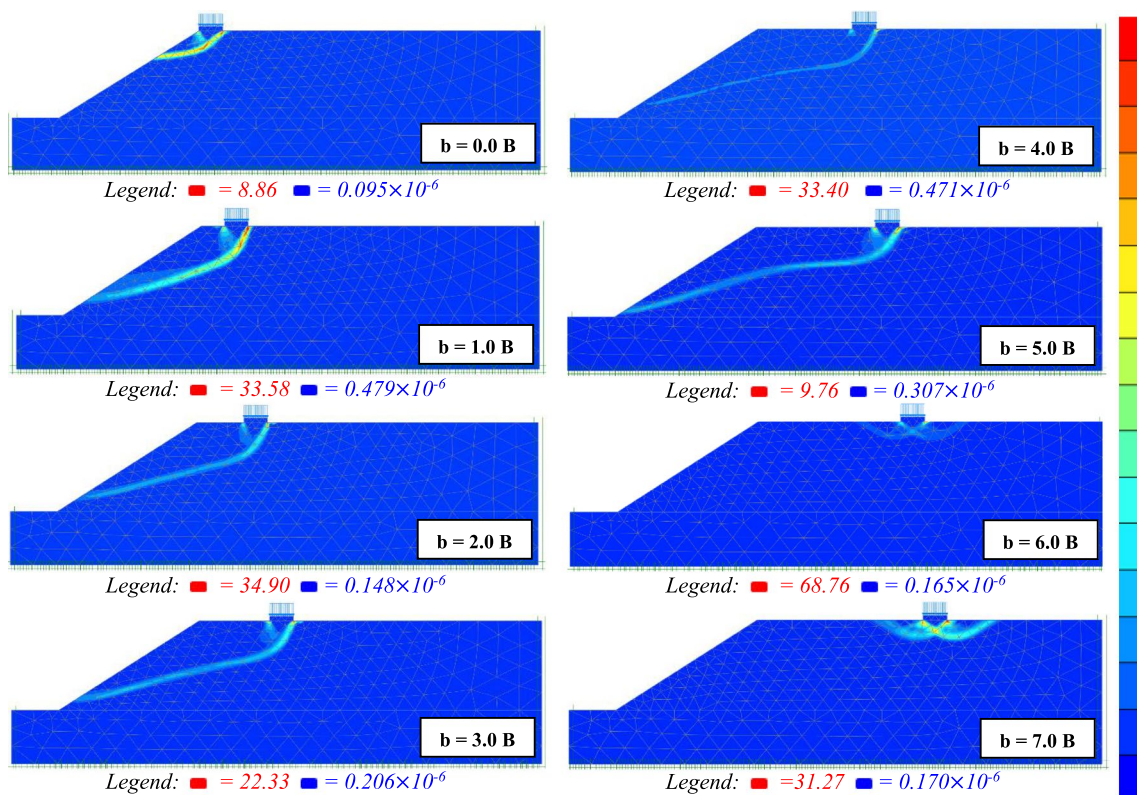


Fig. 16 Failure pattern generated under foundation with b/B ratio ($B=2\text{m}$; $D_f=0.0\text{ B}$; $\phi=40^\circ$; $c=8$; $\beta=40^\circ$)

the contributing independent (input) variables. Thus, sensitivity analysis aids in reducing the model simulations' number without affecting the generality of the conclusions. Many ways to differentiate the critical input variables (parameters) have been referred to in the literature [13, 41]. Garson's algorithm has been employed in the current research to evaluate the relevance of the input parameters. To accomplish this, first, compute the products (Table 9) of the input-hidden (Table 7) and hidden-output (Table 8) connection weights and then, calculate the input parameter importance using the following formula:

$$\text{Input}_X = \sum_{N=1}^5 \frac{|\text{Hidden}_{XN}|}{\sum_{Z=1}^6 |\text{Hidden}_{ZN}|} \quad (\text{Garson's Algorithm}) \quad (1)$$

Table 5 Samples number used for strip foundation analysis

Performance	Division %	No. of samples
Training	70	2756
Validation	15	590
Testing	15	590
Total dataset		3936

where Hidden_{XN} = the absolute connection weight values for input to output nodes, and Hidden_{ZN} = the absolute product connection weights values for the input-hidden and hidden-output nodes.

Figure 20 shows the results of the sensitivity assessment for the presented ANN structure as per Garson's algorithm. It displays that the foundation width, B , the internal friction angle, ϕ° , and soil cohesion, c , are the most relevant impact input parameters on the $q_u/\gamma H$ value of the continuous foundation placed on the earthen slope crest.

Mathematical Expression Development for $(q_u/\gamma H)$

Based on the ANN model's ideal biases and weights obtained from the trained neural network model 6-5-1, a mathematical prediction expression is constructed [15, 36, 42, 43]. As shown in Eq. 2, it connects the input parameters (B , c , ϕ° , D_f/B , β , and b/B) with the output $q_u/\gamma H$ value corresponding to the 5% B settlement.

$$\left(\frac{q_u}{\gamma H} \right) = f_{sig} \left\{ b_o + \sum_{N=1}^h \left[\omega_{Nf_{sig}} (b_{hN} + \sum_{i=1}^m \omega_{iN} X_i) \right] \right\} \quad (2)$$

Table 6 Trials for selection of ANN model structure

Net name	Training function	Learning function	Transfer functions		Net structure	Best validation parameters		
			Input to hidden	Hidden to output		MSE	R ²	Epoch
Network 1	TRIANLM	LEARNGDM	TANSIG	TANSIG	6-1-1	0.1002	0.9503	940
			TANSIG	LOGSIG		1.2662	0.2272	5
			TANSIG	PURELIN		0.0873	0.9504	7
			LOGSIG	TANSIG		0.0957	0.9500	21
			LOGSIG	LOGSIG		1.2662	0.4270	5
Network 2	TRIANLM	LEARNGDM	TANSIG	TANSIG	6-2-1	0.0391	0.9814	345
			TANSIG	PURELIN		0.0388	0.9809	87
			LOGSIG	TANSIG		0.0391	0.9814	302
			LOGSIG	PURELIN		0.0387	0.9810	169
Network 3	TRIANLM	LEARNGDM	TANSIG	TANSIG	6-3-1	0.0185	0.9924	704
			TANSIG	PURELIN		0.0164	0.9929	1073
			LOGSIG	TANSIG		0.0185	0.9924	611
			LOGSIG	PURELIN		0.0165	0.9929	112
Network 4	TRIANLM	LEARNGDM	TANSIG	TANSIG	6-4-1	0.0089	0.9959	218
			TANSIG	PURELIN		0.0147	0.9939	299
			LOGSIG	TANSIG		0.0114	0.9951	166
			LOGSIG	PURELIN		0.0074	0.9969	383
Network 5	TRIANLM	LEARNGDM	TANSIG	TANSIG	6-5-1	0.0051	0.9978	438
			TANSIG	PURELIN		0.0126	0.9945	65
			LOGSIG	TANSIG		0.0073	0.9969	506
			LOGSIG	PURELIN		0.0097	0.9959	54
Network 6	TRIANLM	LEARNGDM	TANSIG	TANSIG	6-6-1	0.0059	0.9975	32
			TANSIG	PURELIN		0.0090	0.9960	83
			LOGSIG	TANSIG		0.0056	0.9977	170
			LOGSIG	PURELIN		0.0079	0.9965	93

where $q_u/\gamma H$ = normalized bearing pressure; X_i = input variables; f_{sig} = Tan-sigmoid transfer function; m = input

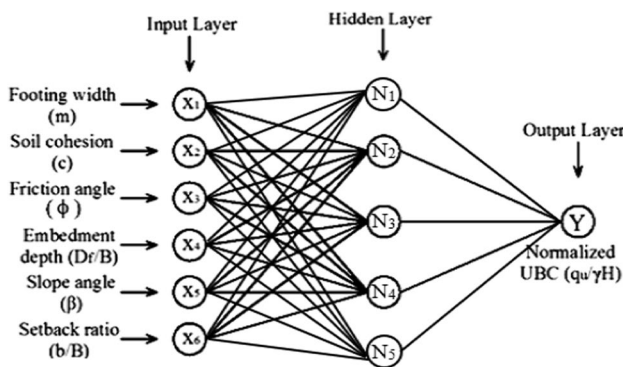


Fig. 17 The ANN model structure (single strip foundation)

variables number; h = hidden layer neurons; ω_{iN} = related weight between the i th input layer and N th node of hidden layer; ω_N = related weight between N th hidden layer node and output node; b_{hN} = the N th hidden layer bias (threshold); and b_o = output layer bias.

The mathematical equation of the ANN model for $q_u/\gamma H$ of the strip foundation placed on the slope crest has been built with the weights and thresholds aid listed in Tables 7 and 8, as per the following expressions:

$$A_1 = -0.0432B - 1.5697c - 0.8625\varphi - 0.1421\left(\frac{D_f}{B}\right) + 0.5150\beta - 0.6604\left(\frac{b}{B}\right) - 3.4056 \tag{3}$$

$$A_2 = -0.1755B - 0.0510c + 0.2370\varphi + 0.0501\left(\frac{D_f}{B}\right) + 0.0149\beta - 0.0224\left(\frac{b}{B}\right) - 0.9481 \tag{4}$$

Fig. 18 Capability of ANN model for training, validation, and testing phases

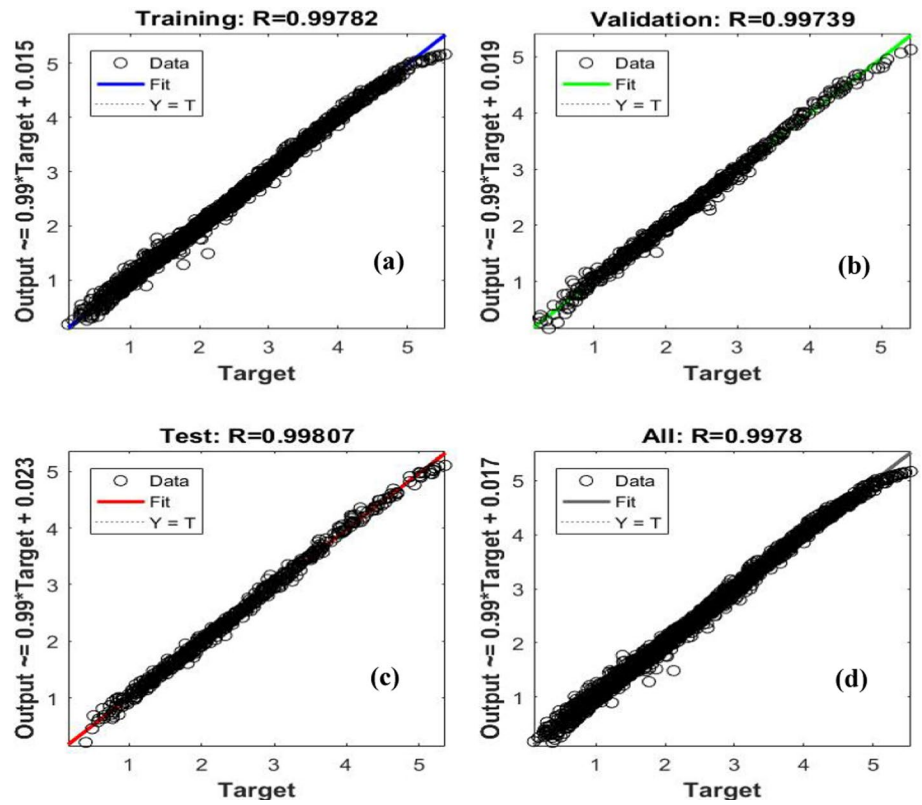


Table 7 Input to hidden weights and thresholds (biases)

X_i	N_1	N_2	N_3	N_4	N_5
B	-0.0432	-0.1755	-2.1060	-3.1733	0.0934
c	-1.5697	-0.0510	-0.0403	0.0360	0.0710
φ^o	-0.8625	0.2370	0.2104	-0.2108	-0.2758
D_f/B	-0.1421	0.0501	0.0501	-0.0545	-0.0535
β	0.5150	0.0149	0.0240	-0.0425	-0.0105
b/B	-0.6604	-0.0224	-0.0467	0.1035	0.0049
b_N	-3.4056	-0.9481	-3.0045	4.9441	0.7550

$$A_3 = -2.106B - 0.0403c + 0.2104\varphi + 0.0501\left(\frac{D_f}{B}\right) + 0.024\beta - 0.0467\left(\frac{b}{B}\right) - 3.0045 \quad (5)$$

$$A_4 = -3.1733B + 0.0360c - 0.2108\varphi - 0.0545\left(\frac{D_f}{B}\right) - 0.0425\beta + 0.1035\left(\frac{b}{B}\right) + 4.9441 \quad (6)$$

$$A_5 = +0.0934B + 0.0710c - 0.2758\varphi - 0.0535\left(\frac{D_f}{B}\right) - 0.0105\beta + 0.0049\left(\frac{b}{B}\right) + 0.7550 \quad (7)$$

$$B_1 = -22.3421(e^{A_1} - e^{-A_1}) / (e^{A_1} + e^{-A_1}) \quad (8)$$

$$B_2 = +183.1677(e^{A_2} - e^{-A_2}) / (e^{A_2} + e^{-A_2}) \quad (9)$$

$$B_3 = -100.4545(e^{A_3} - e^{-A_3}) / (e^{A_3} + e^{-A_3}) \quad (10)$$

$$B_4 = +135.6964(e^{A_4} - e^{-A_4}) / (e^{A_4} + e^{-A_4}) \quad (11)$$

Table 8 Hidden to output weights and thresholds (biases)

Y	N_1	N_2	N_3	N_4	N_5	b_o
$q_u/\gamma H$	-22.3421	183.1677	-100.4545	135.6964	78.9862	-157.3474

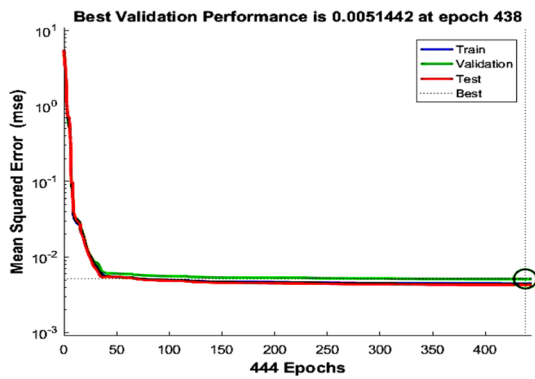


Fig. 19 Best validation performance

Table 9 Input-hidden and hidden-output weights product

X_i	N_1	N_2	N_3	N_4	N_5
B	0.9651	-32.1459	211.5572	-430.6054	7.3737
c	35.0704	-9.3331	4.0437	4.8866	5.6095
ϕ^o	19.2710	43.4162	-21.1346	-28.6062	-21.7852
D_f/B	3.1737	9.1736	-5.0352	-7.3949	-4.2229
β	-11.5053	2.7332	-2.4063	-5.7671	-0.8300
b/B	14.7549	-4.0993	4.6898	14.0473	0.3851

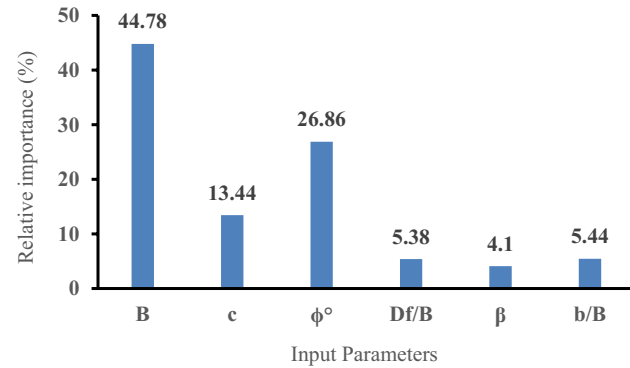


Fig. 20 Rank of input parameters

$$B_5 = +78.9862(e^{A_5} - e^{-A_5}) / (e^{A_5} + e^{-A_5}) \tag{12}$$

$$C_1 = B_1 + B_2 + B_3 + B_4 + B_5 - 157.3474 \tag{13}$$

$$(q_u/\gamma H)_{norm} = (e^{C_1} - e^{-C_1}) / (e^{C_1} + e^{-C_1}) \tag{14}$$

where $(q_u/\gamma H)_{norm}$, in Eq. (14), is the normalized bearing capacity. To compute its value, before subjecting the input data for the parameters in Eqs. (3–7) to the network process,

Table 10 Normalized expressions for the input parameters

Parameter	Normalized expression
B (m)	$B_{norm} = 2B - 3$
c (kPa)	$c_{norm} = 0.05c - 1$
ϕ^o	$\phi_{norm} = 0.0714\phi - 1.8571$
D_f/B	$(D_f/B)_{norm} = 2(D_f/B) - 1$
β^o	$\beta_{norm} = 0.08\beta - 3.8$
b/B	$(b/B)_{norm} = 0.2857(b/B) - 1$

it should be normalized according to the used transfer functions between input and hidden layers (in this work, the TANSIG function is utilized), which normalizes the input parameters between (-1 and +1) as per Eq. (15).

$$P_i^n = \frac{2(P_i^a - P_i^{min})}{(P_i^{max} - P_i^{min})} - 1 \tag{15}$$

where P_i^a and P_i^n are the i th input or target vector components before and after normalization, respectively. P_i^{max} and P_i^{min} are the maximum and minimum values before the normalization of all input or target vector components.

The input and target dataset range of the present study are illustrated in Table 4, and the normalized expressions for the input parameters are displayed in Table 10.

Using the same Eq. (15) above, the final (de-normalized) $q_u/\gamma H$ is calculated as follows:

$$(q_u/\gamma H)_{denorm} = 0.5[(q_u/\gamma H)_{norm} + 1][(q_u/\gamma H)_{max} - (q_u/\gamma H)_{min}] + (q_u/\gamma H)_{min} \tag{16}$$

Substituting the target maximum and minimum values shown in Table 9, the final form of Eq. (16) can be written as follows (See Appendix A for calculation sample):

$$(q_u/\gamma H)_{denorm} = 2.722(q_u/\gamma H)_n + 2.826 \tag{17}$$

EPR Model Results

One of the advantages of EPR is the ability to generate many models for a particular physical problem. This provides the modeler with the resilience to select the appropriate expression from the developed expressions depending on a parametric study or engineering judgment. In this investigation, the model with the fewest terms (for simplicity or decrease in complexity) the highest coefficient of determination (COD = R^2) value, and the lowest MSE (to ensure maximum possible fitness) will be chosen as shown in Fig. 21. As with the ANN technique, the total dataset is divided into three sets: 70% for training, 15% for testing, and 15% of the invisible data in both the training and testing processes to validate the predicted EPR model. Trial-and-error is employed to get

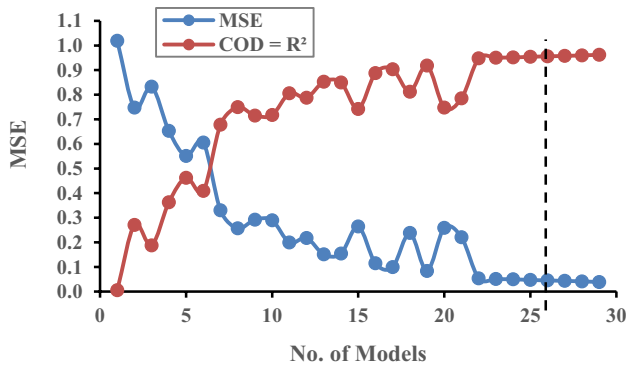


Fig. 21 COD and MSE for developed EPR models

the most effective (optimal) EPR model; Table 11 describes the parameters used to construct the EPR model.

The EPR model calculates the $q_u/\gamma H$ of a continuous foundation situated on an earthen slope crest, using the inputs

Table 11 EPR setting parameters

Parameter	EPR tuning
Expression structure	$Y = \text{sum}(a_i * X_1 * X_2 * f(X_1) * f(X_2)) + a_0$
Function type	No function
Terms	6
Exponents range	0; 0.5; 1; 1.5; 2; -0.5; -1; -1.5; -2
GA parameters	15: 40
Bias (a_0)	yes
Regression method	Non-Negative Least Square
Input parameters	$B, c, \phi, D_f/B, \beta, \text{ and } b/B$

$B, c, \phi, D_f/B, \beta, \text{ and } b/B$. The best EPR model explored in this study to capture the specific geotechnical engineering issue under consideration is summarized in Eq. (18):

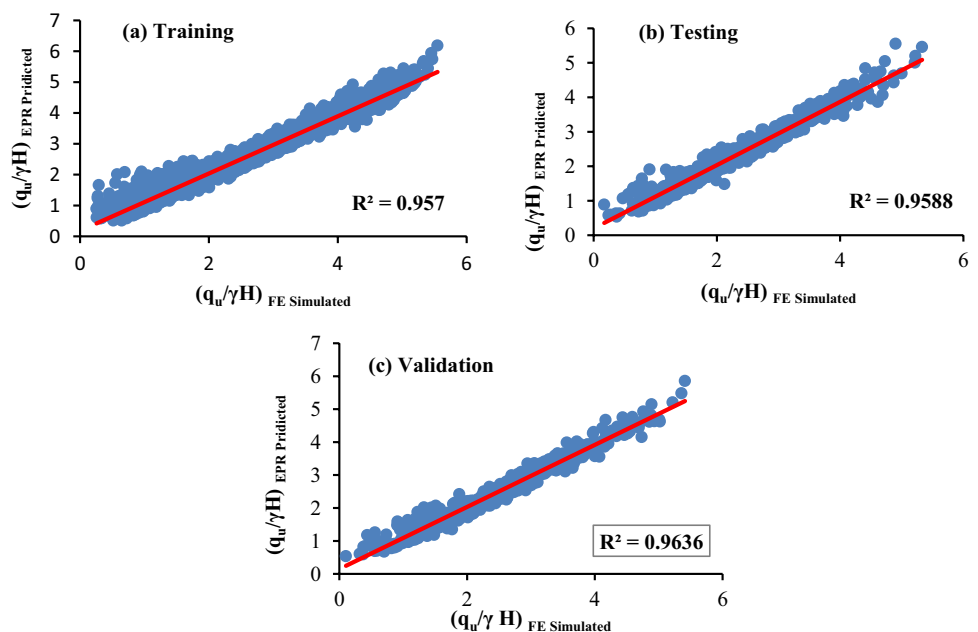
$$\begin{aligned} \frac{q_u}{\gamma H} = & 0.72781 \frac{\phi^2}{\beta^2} + 5.7045 * 10^{-2} \frac{c\phi}{\beta} \\ & + 2.0964 * 10^{-3} B^{0.5} \beta \frac{b}{B} + 3.5021 \frac{B\phi^{0.5} D_f/B}{\beta} \\ & + 1.6175 * 10^{-4} B^{1.5} \phi^2 \left(\frac{b}{B}\right)^{0.5} \end{aligned} \quad (18)$$

Figure 22 displays the comparison of outcomes determined using FE simulation with those predicted by the EPR model (Eq. 18) for the training, testing, and validation phases, respectively, with their corresponding correlation factors. As it appears in the figure, a strong relationship has been indicated between the FE simulation results and those prophesied by the EPR model.

The sensitivity analysis has been done using the one-factor-at-a-time technique, which is considered one of the robust approaches [44] performed to understand the contribution of uncertainty of each input parameter to the model output. This method provides a clear indication of how a single parameter influences the overall outcome. This approach considered the variation range in input parameters of the standard deviation lower and upper than the mean [45]. The sensitivity evaluation results depict that the friction angle, cohesion, and foundation width are the most effective independent variables (inputs) that impact the dependent variable (target) for the proposed model as presented in Fig. 23.

Despite the two different approaches (Garson for ANN model and one-factor-at-a-time for EPR model) used in the

Fig. 22 Results comparison obtained by FE and EPR



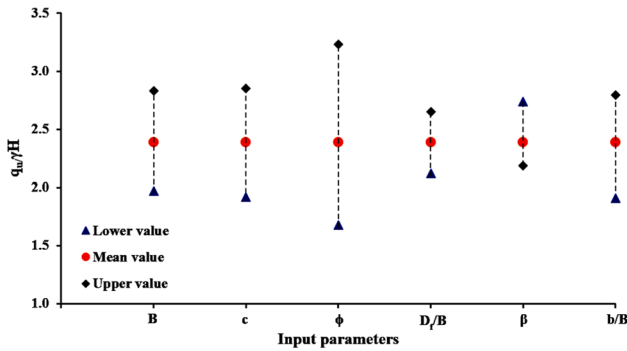


Fig. 23 Sensitivity evaluation of input variables for the EPR model

Table 12 Comparison between ANN and EPR models

Model	Phase	R ²	MSE	VAF	A ¹⁰ -Index
ANN	Training	0.996	0.005	0.996	0.955
	Testing	0.996	0.005	0.995	0.947
	Validation	0.995	0.005	0.996	0.953
	Overall	0.996	0.005	0.996	0.954
EPR	Training	0.957	0.045	0.956	0.905
	Testing	0.959	0.045	0.957	0.893
	Validation	0.964	0.038	0.963	0.905
	Overall	0.958	0.044	0.957	0.903
Perfect value		1	0	1	1

sensitivity analysis of the input variables, the outcomes of both are compatible except for parameters arrangement.

The Distinction Between ANN- and EPR-Developed Models

Table 12 summarizes the performance evaluation of the constructed ANN and EPR models, whereas Table 13 depicts Pearson’s correlation heat map of input and output parameters. According to the stated evaluation indices, the ANN model performance is better than the EPR model in all phases. This indicates that the developed ANN model has more accuracy and capability to generate and predict outcomes than the EPR model, but with a more complex mathematical expression that

Table 13 Pearson’s correlation heat map of input and output parameters

Item	B (m)	c (kPa)	φ°	D _f /B	β°	b/B	(BC) _{FE}	(BC) _{ANN}	(BC) _{EPR}
B (m)	1								
c (kPa)	0	1							
φ°	0	-0.776	1						
D _f /B	0	0	0	1					
β°	0	0.088	0.046	-0.001	1				
b/B	0	0	0	0	0.001	1			
(BC) _{FE}	0.411	-0.132	0.425	0.275	-0.193	0.516	1		
(BC) _{ANN}	0.412	-0.132	0.424	0.276	-0.195	0.518	0.998	1	
(BC) _{EPR}	0.444	-0.163	0.446	0.279	-0.169	0.521	0.979	0.978	1

is difficult to solve manually. This is because ANN does not generate a direct expression, whereas EPR generates a simple and clear mathematical equation that is easily solved manually. So in this regard, the EPR model has superiority over the ANN model. This conclusion is also supported by Fig. 24, which displays Taylor diagrams for both training and testing datasets, due to higher correlation and nearest standard deviation to the simulated FE outcomes.

Zawita Case Study (Duhok City/Kurdistan Region of Iraq)

Site Location and Geology

The investigated area of the Zawita case study is located about 60 km northeast of Duhok city in the Kurdistan Region of Iraq. It is a sub-district of Duhok City. Large parts of the soils in Duhok areas are interspersed with clay beds that vary in color from light brown to reddish brown. This soil is of variable thickness, covering moderately deep inclined rock strata. Duhok geological successions are the Bekhair and Duhok Mountains. Late Cretaceous and Paleocene sediments overlay Bekhair’s anticline. In the northern part of Duhok City, it extends from the southeast toward the northwest, and in the southern part, it extends to Duhok Mountain. The southwestern part of the investigated area is of low relief and dominated mostly by Quaternary deposits. These formations formed from alterations in sand, silt, and clayey silt. Such formations to some extent are unstable from an engineering perspective. So, additional precautions in the design of the foundation are necessary.

Results of Analysis

Figure 25 shows the geometry, boundary conditions, and finite element mesh of the Zawita case study. The FE bearing capacity analysis is conducted using Plaxis 2D in plain strain conditions with a fine element mesh produced by 15-node elements that could result in an extra accurate computation of strain. Whereas Plaxis 2D and SLOPE/W software are used for slope stability analyses. The hardening soil model with a small strain is used to simulate the behavior of the

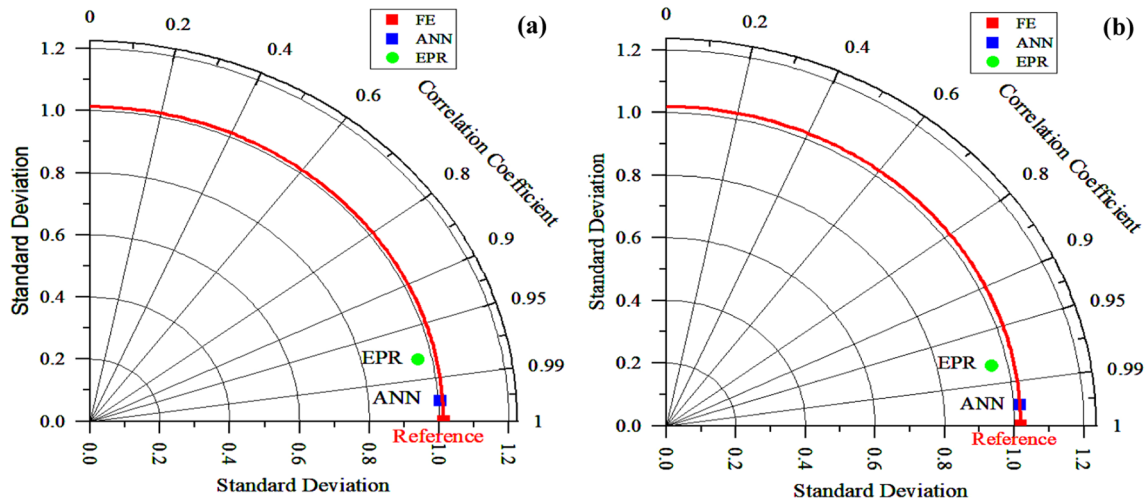


Fig. 24 Taylor diagrams for the developed models, **a** Training data and **b** Testing data

selected slope. The model’s soil and concrete foundation properties are presented in Table 14.

Table 15 shows the bearing pressure results obtained using Plaxis 2D (FEM) for the various conditions of the case

study slope model with those values derived from the ANN and EPR-developed models. The differentiation among the results displays acceptable compatibility despite the soil unit weight and slope angle of the chosen case study being not

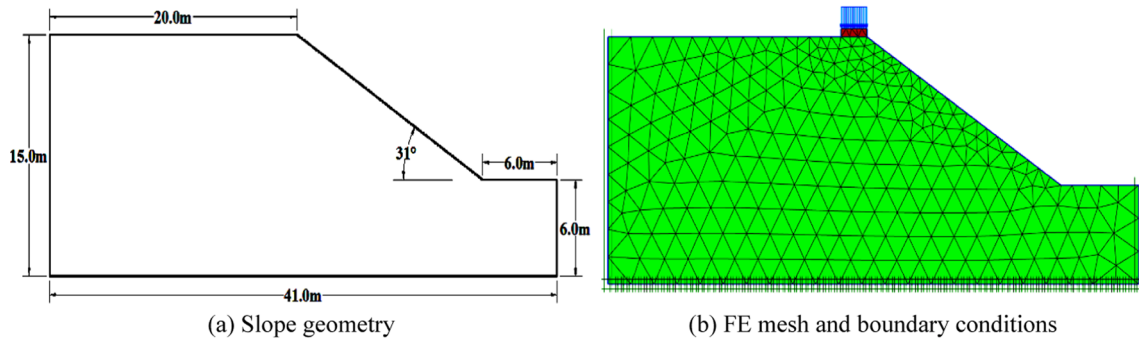


Fig. 25 Slope schematic of Zawita case study

Table 14 Soil and foundation properties of Zawita case study [46]

Parameters	Backfill Material	Concrete foundation	Unit
Material model	HS small	Linear elastic	–
Type of material behavior	Drained	Non-porous	–
Unsaturated unit weight, γ_{unsat}	20.1	24	kN/m ³
Saturated unit weight, γ_{sat}	20.6		kN/m ³
Secant stiffness in standard drained triaxial test, E_{50}^{ref}	3.0×10^4		kN/m ²
Tangent stiffness for primary oedometer loading, E_{oed}^{ref}	3.601×10^4	25×10^6	kN/m ²
Unloading/reloading stiffness, E_{ur}^{ref}	1.108×10^5		kN/m ²
Power for a stress-level dependency on stiffness, m	0.5		–
Cohesion, c'_{ref}	10		kN/m ²
Friction angle, ϕ'	40		°
Dilatancy angle, ψ	10		°
Shear strain at which $G_s = 0.722 G_0, \gamma_{0.7}$	1.5×10^{-4}		–
Shear modulus at very small strains, G_0^{ref}	1.0×10^5		kN/m ²
Poisson’s ratio, ν'_{ur}	0.2	0.15	–

Table 15 Comparison of bearing capacity values (in kPa) at 5.0% B settlement

B (m)	b/B	$D_f/B=0.0$			$D_f/B=0.5$		
		FEM	ANN	EPR	FEM	ANN	EPR
1.0	0.0	323.9	369.7	352.4	378.1	406.5	417.0
	2.0	410.0	441.7	442.1	469.8	487.9	506.7
	4.0	458.9	492.8	493.0	523.9	548.5	557.6
2.0	0.0	390.2	417.3	352.4	504.0	518.3	481.6
	2.0	564.5	574.9	572.9	687.4	693.7	702.1
	4.0	637.3	668.1	683.7	756.2	786.7	812.9

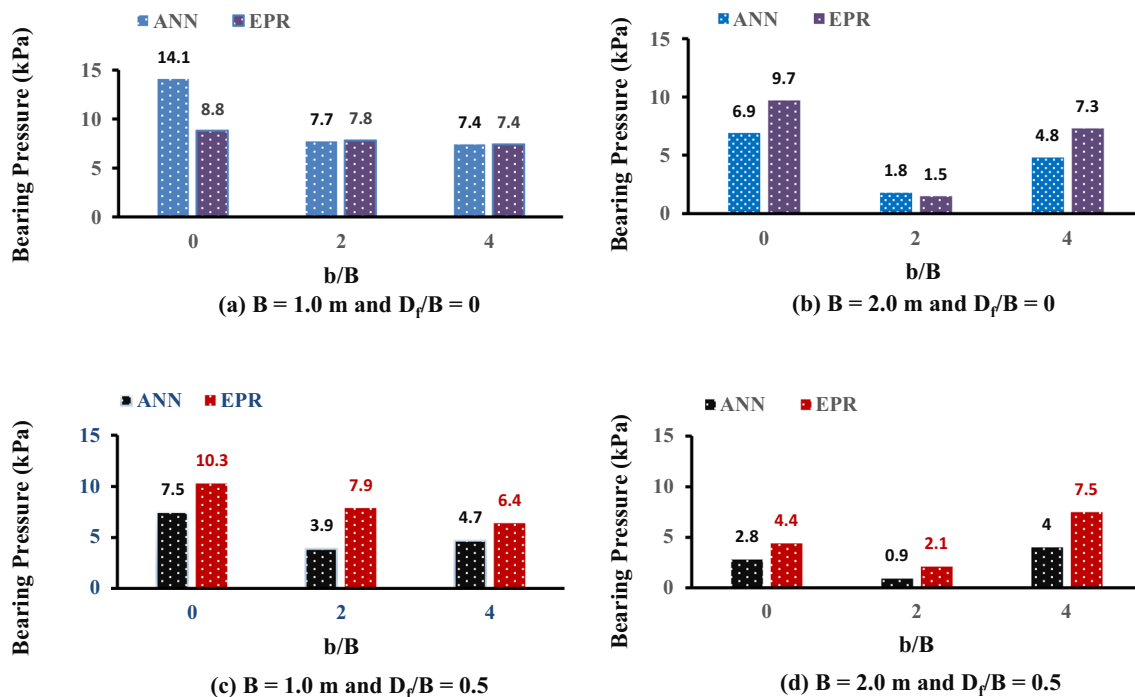
within the data range of the ANN and EPR selected models. It means that the selected models have a high capacity to generate plausible results.

Figure 26 illustrates the differences between ANN and EPR bearing pressure computed by FEM for D_f/B equal to 0 and 0.5. As shown, for $D_f/B=0$, and $B=1$ m, the percentage differences in ANN bearing pressure with FEM are 14.1, 7.7, and 7.4%, for $b/B=0, 2$, and 4, respectively. The same slope status ratios decrease to 6.9, 1.8, and 4.8% when $B=2$ m. Similarly, when $D_f/B=0.5$, and $B=1$ m, the differences with FEM are 7.5, 3.9, and 4.7%, and when $B=2$ m, these ratios decrease to 2.8, 0.9, and 4.0% for the same slope situations. On the other hand, when $D_f/B=0$, and $B=1$ m, the EPR values differ from FEM by 8.8, 7.8, and 7.4%, for $b/B=0, 2$, and 4, respectively. When $B=2$ m, these ratios

decrease to 9.7, 1.5, and 7.3% in similar situations. Also, when $D_f/B=0.5$, and $B=1$ m, the differences with FEM are 10.3, 7.9, and 6.4%, and when $B=2$ m, these ratios decrease to 4.4, 2.1, and 7.5%, for the same b/B , respectively. As is evident from this figure, the average differences between both models are within 6% maximum, indicating that both models are highly accurate.

Based on Fig. 27, the contours of failure patterns developed under the foundation show that the failure is one-sided, toward the slope face, due to eliminating the passive zone.

Tables 16 and 17 and Fig. 28 depict the safety factor FOS of the slope stability analysis for various slope conditions of the case study using many approaches (FEM, Bishop, Morgenstern-Price, and Spencer). It was observed that for slope angle $\beta = 31^\circ$ and any foundation width considered,

**Fig. 26** ANN and EPR bearing capacity percentage differences from FEM

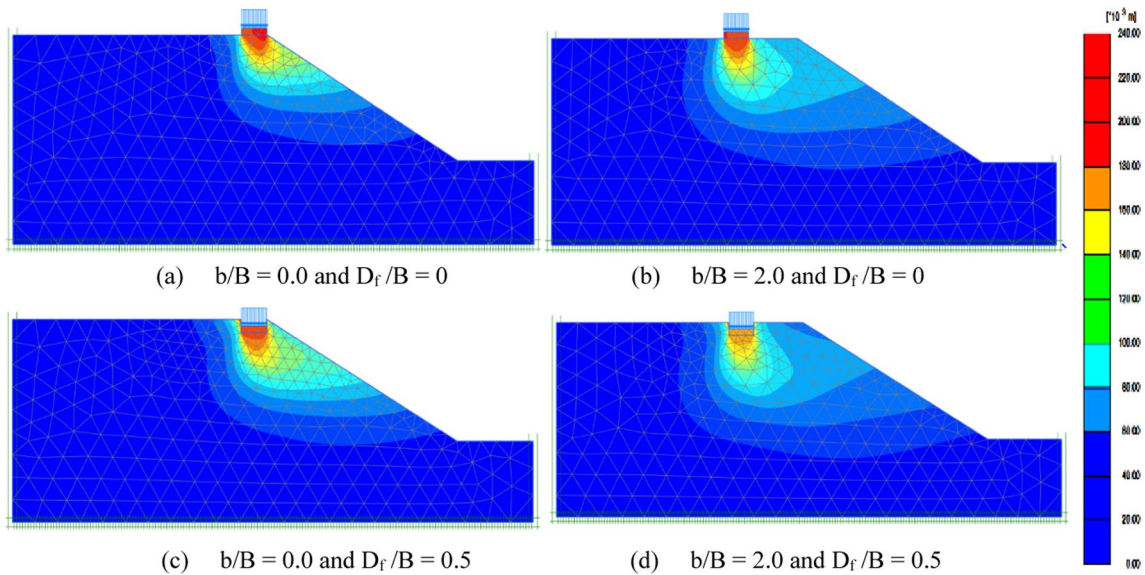


Fig. 27 Contours of failure patterns generated under the foundation of some case study situations

Table 16 Safety factors for Zawita case study without loading

FEM	Limit Equilibrium Methods (LEM)		
	Bishop	M-P	Spencer
2.215	2.269	2.262	2.261

a much wider and deeper zone of critical failure, and as a result revealed higher concentrations of plastic strain near the top of the slope. Also, LE methods do not consider the fundamental aspects of the stress–strain relationship, and thus, they cannot compute a realistic stress distribution [47, 48]. A comparison of LE methods considered in this study shows that safety factors calculated by the Simplified Bishop Method are approximately 2–4% lower than those obtained by other methods. However, it cannot be accepted for complex slopes with multiple failure factors, since it does not take into account interslice forces compared to Spencer’s or Morgenstern and Price’s methods that satisfy both force and moment equilibrium.

the FOS increases as the footing setback b/B distance increases. The same trend was noticed in all analysis methods. Table 17 shows that FEM yields a lower FOS value than all LE methods. This is attributed to their fundamentally different approaches. Hence, the LE methods have more limitations than the FEM, resulting in a relatively defined critical failure surface, whereas the FEM showed

Table 17 Safety factors for Zawita case study at load corresponding to 5.0% B settlement

B (m)	b/B	$D_f/B=0.0$				$D_f/B=0.5$			
		FEM	Limit equilibrium methods			FEM	Limit equilibrium methods		
			Bishop	M-P	Spencer		Bishop	M-P	Spencer
1	0	1.139	1.17	1.189	1.199	1.185	1.415	1.443	1.34
	2	1.342	1.477	1.505	1.54	1.376	1.625	1.638	1.705
	4	1.458	1.837	1.836	1.879	1.542	1.87	1.87	1.906
2	0	1.11	1.107	1.128	1.144	1.185	1.39	1.417	1.355
	2	1.317	1.538	1.566	1.594	1.373	1.653	1.664	1.694
	4	1.45	1.908	1.909	1.898	1.562	1.955	1.962	1.986

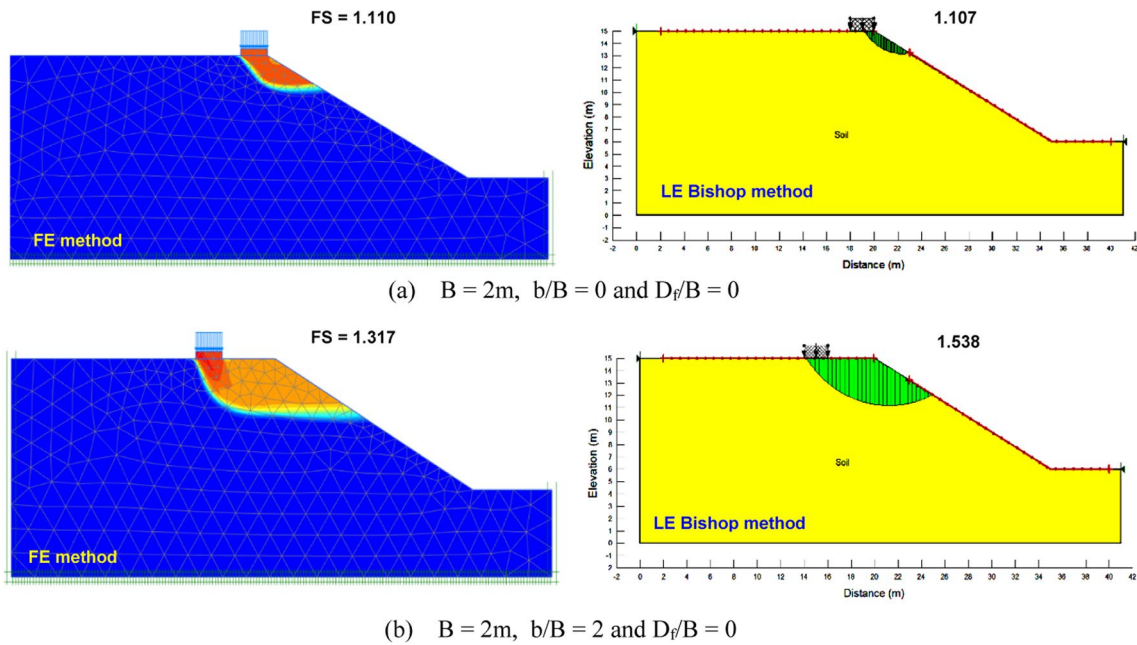


Fig. 28 Some case study stability analysis at q corresponding to 5% B settlement

Conclusions

This investigation presents two models using ANN and EPR techniques to predict the normalized bearing pressure $q_u/\gamma H$ from data obtained by FE simulation of a continuous foundation on the earthen slope crest using different geometrical and geotechnical parameters such as (B , c , ϕ , D_f/B , β , and b/B). It is worth mentioning that the developed expressions are valid and accurate within the range of the parameters considered in this study, but outside of these limits, the foretelling must be validated. The following conclusions are drawn from the outcomes:

- The bearing capacity improved as B , c , ϕ , D_f/B , and b/B increased but it negatively related to β .
- The critical b/B ratio was found to be 6, after which the slope inclination influence vanished, and the foundation behaved like it was placed on the horizontal ground.
- The FOS increases as the foundation setback increases to reach the critical b/B ratio.
- The ANN and EPR techniques offer the best capable models to forecast the $q_u/\gamma H$ of the strip foundation

situated on the slope crest, based on the high R^2 values achieved in the training, validation, and testing phases.

- The prediction precision of ANN and EPR models is close to each other; however, the EPR model can directly give a simple mathematical equation that is easily solved manually without needing to use any software, whereas the ANN model provides a complex expression that is difficult to solve manually.
- Based on the optimum weights and thresholds obtained from ANN and the more appropriate EPR model, an adequate mathematical expression for predicting $q_u/\gamma H$ of strip foundations located on the slope crest has been provided. This mathematical prediction expression will serve as a simple and quick tool for the geotechnical practicing and consulting engineers included in the hilly area planning and design.
- The sensitivity analysis using Garson's technique indicated that the most important parameters that affect the $q_u/\gamma H$ value are B , ϕ , and c .
- The results of the selected case study proved that the chosen models of ANN and EPR are powerful and give acceptable results.

Funding This research received no specific grant from any funding agency, commercial or not-for-profit sectors.

Declarations

Conflict of interest The authors have no financial or personal affiliations with any of the products, services, or corporations mentioned in this paper.

Appendix A: ANN case study result calculation sample

<i>B</i> (m)	<i>c</i> kN/m ²	ϕ°	<i>D_f/B</i>	β°	<i>b/B</i>
2	10	40	0	31	0

Geometry and soil parameters.

The normalized input parameters in the range (− 1, + 1) according to Table 10.

Parameter	Normalized expression	Normalized input parameter values
<i>B</i> (m)	$B_{norm} = 2B - 3$	$= 2(2) - 3 = 1$
<i>c</i> (kPa)	$c_{norm} = 0.05c - 1$	$= 0.05(10) - 1 = -0.5$
ϕ°	$\phi_{norm} = 0.0714\phi - 1.8571$	$= 0.0714(40) - 1.8571 = 0.985$
<i>D_f/B</i>	$(D_f/B)_{norm} = 2(D_f/B) - 1$	$= 2(0) - 1 = -1$
β°	$\beta_{norm} = 0.08\beta - 3.8$	$= 0.08(31) - 3.8 = -1.32$
<i>b/B</i>	$(b/B)_{norm} = 0.2857(b/B) - 1$	$= 0.2857(0) - 1 = -1$

Weights and bias for input-hidden layers from Table 6

Hidden layer no	<i>B</i>	<i>c</i>	ϕ°	<i>D_f/B</i>	β°	<i>b/B</i>	Bias
N ₁	− 0.0432	− 1.5697	− 0.8625	− 0.1421	0.5150	− 0.6604	− 3.4056
N ₂	− 0.1755	− 0.0510	0.2370	0.0501	0.0149	− 0.0224	− 0.9481
N ₃	− 2.1060	− 0.0403	0.2104	0.0501	0.0240	− 0.0467	− 3.0045
N ₄	− 3.1733	0.0360	− 0.2108	− 0.0545	− 0.0425	0.1035	4.9441
N ₅	0.0934	0.0710	− 0.2758	− 0.0535	− 0.0105	0.0049	0.7550

$$A1 = -0.0432 * (1) - 1.5697 * (-0.5) - 0.8625 * (0.985) - 0.1421 * (-1) + 0.515 * (-1.32) - 0.6604 * (-1) - 3.4056 = -3.403$$

$$A2 = -0.1755 * (1) - 0.051 * (-0.5) + 0.2370 * (0.985) + 0.0501 * (-1) + 0.0149 * (-1.32) - 0.0224 * (-1) - 0.9481 = -0.909$$

$$A3 = -2.106 * (1) - 0.0403 * (-0.5) + 0.2104 * (0.985) + 0.0501 * (-1) + 0.024 * (-1.32) - 0.0467 * (-1) - 3.0045 = -4.915$$

$$A4 = -3.1733 * (1) + 0.036 * (-0.5) + 0.2108 * (0.985) - 0.0545 * (-1) - 0.0425 * (-1.32) + 0.1035 * (-1) + 4.9441 = 1.549$$

$$A5 = 0.0934 * (1) + 0.071 * (-0.5) - 0.2758 * (0.985) - 0.0535 * (-1) - 0.0105 * (-1.32) + 0.0049 * (-1) + 0.755 = 0.600$$

Weights and bias for hidden-output layers from Table 7

N ₁	N ₂	N ₃	N ₄	N ₅	Bias
− 22.3421	183.1677	− 100.4545	135.6964	78.9862	− 157.3474

(*q_u/γH*)

Min	0.104
Max	5.548

$$B_1 = -22.3421(e^{A_1} - e^{-A_1}) / (e^{A_1} + e^{-A_1}) = 22.293$$

$$B_2 = +183.1677(e^{A_2} - e^{-A_2}) / (e^{A_2} + e^{-A_2}) = -131.976$$

$$B_3 = -100.4545(e^{A_3} - e^{-A_3}) / (e^{A_3} + e^{-A_3}) = 100.444$$

$$B_4 = +135.6964(e^{A_4} - e^{-A_4}) / (e^{A_4} + e^{-A_4}) = 123.982$$

$$B_5 = +78.9862(e^{A_5} - e^{-A_5}) / (e^{A_5} + e^{-A_5}) = 42.412$$

$$C_1 = B_1 + B_2 + B_3 + B_4 + B_5 - 157.3474 = (22.293 - 132.976 + 100.444 + 123.982 + 42.412) - 157.3474 = -0.193$$

$$(q_u/\gamma H)_{norm} = (e^{C_1} - e^{-C_1}) / (e^{C_1} + e^{-C_1}) = -0.191$$

$$(q_u/\gamma H)_{denorm} = 0.5[(q_u/\gamma H)_{norm} + 1](q_u/\gamma H)_{max} - (q_u/\gamma H)_{min} + (q_u/\gamma H)_{min} = 2.307$$

$$\begin{aligned}(q_u)_{denorm} &= 2.307(\gamma H) = 2.307(20.1)(9) \\ &= 417.3 \text{ kN/m}^2, (\text{See Table 14}).\end{aligned}$$

References

- Meyerhof GG (1963) Some recent research on the bearing capacity of foundations. *Can Geotech J* 1(1):16–26. <https://doi.org/10.1139/t63-003>
- Hansen JB (1970) A revised and extended formula for bearing capacity. Danish Geotechnical Institute.
- Castelli F, Lentini V (2012) Evaluation of the bearing capacity of footings on slopes. *Int J Phys Modell Geotech* 12(3):112–118. <https://doi.org/10.1680/ijpmg.11.00015>
- Salih Keskin M, Laman M (2013) Model studies of bearing capacity of strip footing on sand slope. *KSCE J Civil Eng* 17(4):699–711. <https://doi.org/10.1007/s12205-013-0406-x>
- Meyerhof G (1957) The ultimate bearing capacity of foundations on slopes. In: *Proc., 4th Int. Conf. on Soil Mechanics and Foundation Engineering*
- Narita K, Yamaguchi H (1990) Bearing capacity analysis of foundations on slopes by use of log-spiral sliding surfaces. *Soils Found* 30(3):144–152. https://doi.org/10.3208/sandf1972.30.3_144
- Georgiadis K (2010) Undrained bearing capacity of strip footings on slopes. *J Geotech Geoenviron Eng* 136(5):677–685. [https://doi.org/10.1061/\(ASCE\)GT.1943-5606.0000269](https://doi.org/10.1061/(ASCE)GT.1943-5606.0000269)
- Leshchinsky B (2015) Bearing capacity of footings placed adjacent to slopes. *J Geotech Geoenviron Eng* 141(6):04015022–04015113. [https://doi.org/10.1061/\(ASCE\)GT.1943-5606.0001306](https://doi.org/10.1061/(ASCE)GT.1943-5606.0001306)
- Leshchinsky B, Xie Y (2017) Bearing capacity for spread footings placed near c' - ϕ' slopes. *J Geotech Geoenviron Eng* 143(1):06016020. [https://doi.org/10.1061/\(ASCE\)GT.1943-5606.0001578](https://doi.org/10.1061/(ASCE)GT.1943-5606.0001578)
- Acharyya R, Dey A, Kumar B (2020) Finite element and ANN-based prediction of bearing capacity of square footing resting on the crest of c - ϕ soil slope. *Int J Geotech Eng* 14(2):176–187. <https://doi.org/10.1080/19386362.2018.1435022>
- Gao Z, Zhao J, Li X (2021) The deformation and failure of strip footings on anisotropic cohesionless sloping grounds. *Int J Numer Anal Meth Geomech* 45(10):1526–1545. <https://doi.org/10.1002/nag.3212>
- Shahin MA, Jaksa MB, Maier HR (2002) Artificial neural network based settlement prediction formula for shallow foundations on granular soils. *Aust Geomech J News Aust Geomech Soc* 37(4):45–52
- Shahin MA, Maier HR, Jaksa MB (2002) Predicting settlement of shallow foundations using neural networks. *J Geotech Geoenviron Eng* 128(9):785–793. [https://doi.org/10.1061/\(ASCE\)1090-0241\(2002\)128:9\(785\)](https://doi.org/10.1061/(ASCE)1090-0241(2002)128:9(785))
- Kuo YL et al (2009) ANN-based model for predicting the bearing capacity of strip footing on multi-layered cohesive soil. *Comput Geotech* 36(3):503–516. <https://doi.org/10.1016/j.compgeo.2008.07.002>
- Behera RN et al (2013) Prediction of ultimate bearing capacity of eccentrically inclined loaded strip footing by ANN, part I. *Int J Geotech Eng* 7(1):36–44. <https://doi.org/10.1179/1938636212Z.0000000012>
- Behera RN et al (2013) Prediction of ultimate bearing capacity of eccentrically inclined loaded strip footing by ANN: Part II. *Int J Geotech Eng* 7(2):165–172. <https://doi.org/10.1179/1938636212Z.0000000019>
- Zhu Y et al (2022) Estimation of splitting tensile strength of modified recycled aggregate concrete using hybrid algorithms. *Steel Compos Struct* 44(3):389–406. <https://doi.org/10.12989/scs.2022.44.3.389>
- Esmaeili-Falak M, Benemaran RS (2023) Ensemble deep learning-based models to predict the resilient modulus of modified base materials subjected to wet-dry cycles. *Geomech Eng* 32(6):583–600. <https://doi.org/10.12989/gae.2023.32.6.583>
- Dawei Y et al (2023) Predicting the CPT-based pile set-up parameters using HHO-RF and PSO-RF hybrid models. *Struct Eng Mech* 86(5):673–686. <https://doi.org/10.12989/sem.2023.86.5.673>
- Acharyya R (2019) Finite element investigation and ANN-based prediction of the bearing capacity of strip footings resting on sloping ground. *Int J Geo-Eng* 10(1):1–19. <https://doi.org/10.1186/s40703-019-0100-z>
- Acharyya R, Dey A (2019) Assessment of bearing capacity for strip footing located near sloping surface considering ANN model. *Neural Comput Appl* 31(11):8087–8100. <https://doi.org/10.1007/s00521-018-3661-4>
- Ebid AM, Onyelowe KC, Arinze EE (2021) Estimating the ultimate bearing capacity for strip footing near and within slopes using AI (GP, ANN, and EPR) techniques. *J Eng* 2021:3267018. <https://doi.org/10.1155/2021/3267018>
- Shahin MA (2015) Use of evolutionary computing for modelling some complex problems in geotechnical engineering. *Geomech Geoeng* 10(2):109–125. <https://doi.org/10.1080/17486025.2014.921333>
- Asr AA, Faramarzi A, Javadi AA (2018) An evolutionary modelling approach to predicting stress-strain behaviour of saturated granular soils. *Eng Comput*. <https://doi.org/10.1108/EC-01-2018-0025>
- Karimpour Fard M, Mashmouli Juybari R, Rezaie Soufi G (2020) Evolutionary polynomial regression-based models for the one-dimensional compression of Chamkhaleh sand mixed with EPS and tire derived aggregate. *AUT J Civil Eng* 4(3):323–332. <https://doi.org/10.22060/ajce.2019.16381.5583>
- Chavda JT, Dodagoudar GR (2018) Finite element evaluation of ultimate capacity of strip footing: Assessment using various constitutive models and sensitivity analysis. *Innovat Infrastruct Solut* 3(1):15. <https://doi.org/10.1007/s41062-017-0121-4>
- Alzabeebee S (2022) A comparative study of the effect of the soil constitutive model on the seismic response of buried concrete pipes. *J Pipeline Sci Eng* 2(1):87–96. <https://doi.org/10.1016/j.jpse.2021.07.001>
- Abbas JM (2014) Slope stability analysis using numerical method. *J Appl Sci* 14(9):846–859. <https://doi.org/10.3923/jas.2014.846.859>
- Ahmadi M, Asakereh A (2015) Numerical analysis of the bearing capacity of strip footing adjacent to slope. *Int J Sci Eng Investigat* 4(46):49–53. <https://doi.org/10.14445/22315381/IJETT-V29P258>
- Acharyya R, Dey A (2021) Assessment of bearing capacity and failure mechanism of single and interfering strip footings on sloping ground. *Int J Geotech Eng* 15(7):822–833. <https://doi.org/10.1080/19386362.2018.1540099>
- Abed AH, Hameed AM (2016) The Optimum location of reinforcement embankment using 3D plaxis software. *Int J Civil Eng Technol* 7(5):284–291
- Lee K, Manjunath V (2000) Experimental and numerical studies of geosynthetic-reinforced sand slopes loaded with a footing. *Can Geotech J* 37(4):828–842. <https://doi.org/10.1139/t00-016>

33. Sungkar M et al. (2020) Slope stability analysis using Bishop and finite element methods. In: IOP conference series: materials science and engineering. IOP Publishing.
34. Alkroosh I, Nikraz H (2012) Predicting axial capacity of driven piles in cohesive soils using intelligent computing. *Eng Appl Artif Intell* 25(3):618–627. <https://doi.org/10.1016/j.engappai.2011.08.009>
35. Mishra A, Kumar B, Dutta J (2016) Prediction of hydraulic conductivity of soil bentonite mixture using hybrid-ANN approach. *J Environ Inform.* <https://doi.org/10.3808/jei.201500292>
36. Das SK, Basudhar PK (2008) Prediction of residual friction angle of clays using artificial neural network. *Eng Geol* 100(3):142–145. <https://doi.org/10.1016/j.enggeo.2008.03.001>
37. Giustolisi O, Savic DA (2006) A symbolic data-driven technique based on evolutionary polynomial regression. *J Hydroinf* 8(3):207–222. <https://doi.org/10.2166/hydro.2006.020b>
38. Giustolisi O et al (2007) A multi-model approach to analysis of environmental phenomena. *Environ Model Softw* 22(5):674–682. <https://doi.org/10.1016/j.envsoft.2005.12.026>
39. Golberg DE (1989) Genetic algorithms in search, optimization, and machine learning. Addison wesley 1989(102):36
40. Ahangar-Asr A et al (2014) Lateral load bearing capacity modelling of piles in cohesive soils in undrained conditions: An intelligent evolutionary approach. *Appl Soft Comput* 24:822–828. <https://doi.org/10.1016/j.asoc.2014.07.027>
41. Olden JD, Joy MK, Death RG (2004) An accurate comparison of methods for quantifying variable importance in artificial neural networks using simulated data. *Ecol Model* 178(3):389–397. <https://doi.org/10.1016/j.ecolmodel.2004.03.013>
42. Das SK, Samui P, Sabat AK (2011) Application of artificial intelligence to maximum dry density and unconfined compressive strength of cement stabilized soil. *Geotech Geol Eng* 29(3):329–342. <https://doi.org/10.1007/s10706-010-9379-4>
43. Acharyya R, Dey A (2018) Assessment of bearing capacity of interfering strip footings located near sloping surface considering artificial neural network technique. *J Mt Sci* 15(12):2766–2780. <https://doi.org/10.1007/s11629-018-4986-2>
44. Hamby DM (1994) A review of techniques for parameter sensitivity analysis of environmental models. *Environ Monit Assess* 32(2):135–154. <https://doi.org/10.1007/BF00547132>
45. John Bailer A (2001) Probabilistic techniques in exposure assessment. A handbook for dealing with variability and uncertainty in models and inputs. A. C. Cullen and H. C. Frey, Plenum Press, New York and London, 1999. No. of pages: ix + 335. Price: \$99.50. ISBN 0-306-45956-6. Statistics in Medicine, 2001. 20(14): p. 2211–2213 DOI: <https://doi.org/10.1002/sim.958>.
46. Mohammed RA (2018) Experimental and numerical modeling of slope stability for partial saturated soils. In: Civil Engineering. University of Mosul. Iraq: University of Mosul. Iraq.
47. Khabbaz H, Fatahi B, Nucifora C (2012) Finite element methods against limit equilibrium approaches for slope stability analysis. In: Australia New Zealand Conference on Geomechanics. 2012. Geomechanical Society and New Zealand Geotechnical Society.
48. Memon Y (2018) A comparison between limit equilibrium and finite element methods for slope stability analysis. Missouri University of Science and Technology, Rolla, MO, United States DOI: <https://doi.org/10.13140/RG.2.2.16932.53124>.

Publisher's Note Springer Nature remains neutral with regard to jurisdictional claims in published maps and institutional affiliations.

Springer Nature or its licensor (e.g. a society or other partner) holds exclusive rights to this article under a publishing agreement with the author(s) or other rightsholder(s); author self-archiving of the accepted manuscript version of this article is solely governed by the terms of such publishing agreement and applicable law.